Materials Today Bio 32 (2025) 101742

Contents lists available at ScienceDirect

Materials Today Bio

journal homepage: www.journals.elsevier.com/materials-today-bio

Nanoscale piezoelectric patches preserve electrical integrity of infarcted hearts

Luís M. Monteiro [a,b,c,e,1], Pedro J. Gouveia [b], Francisco Vasques-Nóvoa [d,e,f], Susana Rosa [b], Ifigeneia Bardi [g], Rita N. Gomes [e,f,h], Simão Correia-Santos [a,b,c], Leonardo Ricotti [i,j], Lorenzo Vannozzi [i,j], Daniele Guarnera [i,j], Liliana Costa [d], André M. Leite-Moreira [d], Pedro Mendes-Ferreira [d], Adelino F. Leite-Moreira [d], Filippo Perbellini [g], Cesare M. Terracciano [g], Perpétua Pinto-do-Ó [e,f,h], Lino Ferreira [b,k,2,*], Diana S. Nascimento [e,f,h,2,**]

[a] IIIUC-Institute of Interdisciplinary Research, University of Coimbra, Casa Costa Alemão, 3030-789, Coimbra, Portugal
[b] CNC-Center for Neuroscience and Cell Biology, CIBB-Centre for Innovative Biomedicine and Biotechnology, University of Coimbra, UC, Biotech Parque Tecnológico de Cantanhede, 3060-197, Coimbra, Portugal
[c] PhD Programme in Experimental Biology and Biomedicine, Institute for Interdisciplinary Research (IIIUC), University of Coimbra, Casa Costa Alemão, 3030-789, Coimbra, Portugal
[d] UnIC@RISE, Department of Surgery and Physiology, Faculty of Medicine of the University of Porto, Porto, Portugal
[e] i3S - Instituto de Investigação e Inovação em Saúde, Universidade do Porto, Porto, Portugal
[f] INEB - Instituto Nacional de Engenharia Biomédica, Universidade do Porto, Porto, Portugal
[g] Imperial College London, National Heart & Lung Institute, London, United Kingdom
[h] ICBAS - Instituto de Ciências Biomédicas de Abel Salazar, Universidade do Porto, Porto, Portugal
[i] The BioRobotics Institute, Scuola Superiore Sant'Anna, Piazza Martiri della Libertà 33, 56127, Pisa, Italy
[j] Department of Excellence in Robotics & AI, Scuola Superiore Sant'Anna, Piazza Martiri della Libertà 33, 56127, Pisa, Italy
[k] Faculty of Medicine of the University of Coimbra, 3000-548, Coimbra, Portugal

ARTICLE INFO

Keywords:
Cardiac tissue engineering
Cardiac patch
Myocardial infarction
Piezoelectric materials
Electrical integrity
Electroactive patch

ABSTRACT

Ischemic heart disease is the leading cause of death worldwide. Several approaches have been explored to restore cardiac function, however few investigated new strategies to improve electrical functional recovery. Herein, we have investigated the impact of piezoelectric patches (Piezo patches), capable of generating electric charges upon mechanical deformation, on rat cardiac slices, healthy and ischemic hearts (*ex vivo*), on infarcted mice (*in vivo*) and on healthy and infarcted pigs (*in vivo*). Piezo patches did not preclude cardiac slice contractility, while compared with electrically inert control patches. In addition, Piezo patches showed an adequate safety profile in a working heart model as no electrophysiologic alterations were detected in healthy hearts. Epicardial implantation of Piezo patches in acutely infarcted mice hearts significantly improved myocardial electrical integrity without disturbing systolic function. Moreover, Piezo patches partially prevented ischemia-related adverse cardiac remodeling, reducing left ventricular chamber dilatation and compensatory hypertrophy. Coherently, Piezo patch-implanted hearts revealed downregulation of genes associated with extracellular matrix remodeling. Importantly, *in vivo* implantation of Piezo patches in porcine hearts revealed to be electrically safe as no major effects in its electrophysiology were detected. Overall, the results presented here endorse Piezo patches as a promising therapeutic strategy to improve post-myocardial infarction structural and electrical remodeling.

* Corresponding author. CNC-Center for Neuroscience and Cell Biology, CIBB-Centre for Innovative Biomedicine and Biotechnology, University of Coimbra, UC, Biotech Parque Tecnológico de Cantanhede, 3060-197, Coimbra, Portugal.
** Corresponding author. i3S- Instituto de Investigação e Inovação em saúde, ICBAS - Instituto de Ciências Biomédicas de Abel Salazar, Universidade do Porto, Porto, Portugal.
E-mail addresses: lino.ferreira@uc.pt (L. Ferreira), dsn@i3s.up.pt (D.S. Nascimento).
[1] Author currently employed by Univ. Bordeaux, INSERM, CRCTB, U 1045, IHU Liryc, F-33000 Bordeaux, France.
[2] Senior co-leading authors with equal contributions.

https://doi.org/10.1016/j.mtbio.2025.101742
Received 4 February 2025; Received in revised form 27 March 2025; Accepted 6 April 2025
Available online 9 April 2025

1. Introduction

Myocardial infarction (MI) is a leading cause of disability and death [1]. Innovative cellular [2] and non-cellular [3] regenerative approaches for MI have been described in the last 20 years, although with limited clinical impact. Since 2004, several research groups have explored the use of biomaterial-based approaches to treat MI [4]. These biomaterials may be injected in the heart or delivered as cardiac patches through minimally invasive strategies [5]. The results collected in pre-clinical tests showed that some biomaterials were able to prevent adverse left ventricle (LV) remodeling by reducing infarct wall thinning, infarct size and LV dilatation [4]. To improve electromechanical functional recovery after MI conductive cardiac patches have been investigated [6–10]. Although this strategy has been recently shown to improve cardiac function (both systolic and electrophysiological) and to attenuate maladaptive cardiac remodeling upon MI in rodents [9,10], others studies have shown evidence that conductive patches could reduce myocardial contractility (when applied in cardiac slices) [6,7].

Electrical stimulation of the infarcted heart constitutes an exploratory approach to improve electromechanical functional recovery after MI [11]. Currently, that would imply the use of external electrical stimulation, which is impractical, or the use of electronic devices such as implantable cardioverter defibrillators (ICDs) that, despite being well-established, have limited battery life, exhibit safety risks and are only designed to prevent arrhythmia-induced sudden cardiac deaths and not to improve cardiac function [12,13]. Piezoelectric materials may represent a more practical and effective solution. A given material is considered piezoelectric when it exhibits an electrical polarization (and a corresponding generation of electrical charges) upon mechanical stress (direct effect) or vice-versa (converse effect) [14]. Although most common applications for piezoelectric materials are related to electronics and sensors, biomedical applications for these materials have been encouraged [15,16] due to their inherent potential to provide electrical stimuli in the absence of an external electrical source by harnessing body movements, added to the fact that some biological tissues naturally exhibit piezoelectric properties (e.g. bone, tendons) [17–20]. In tissue engineering, piezoelectric materials have been studied in the context of bone and neural tissue, where the most commonly used composites include lead zirconate titanate, poly(vinylidene fluoride) (PVDF) and its co-polymers [21,22].

Piezoelectric materials have been tested *in vitro* with cardiomyocytes [23,24] to enhance their contractility and maturation. Indeed, we have shown that poly(caprolactone) (PCL) nanofilms coated with piezoelectric nanofibers of PVDF–trifluoroethylene (PVDF-TrFE) sustained rat and human cardiomyocyte viability, alignment and contractility *in vitro* for at least 12 days, and contribute for cell maturation as measured by the upregulation of relevant ionic channel subunits and connexin 43 [24]. Regarding the cardiac *in vivo* application of these materials,

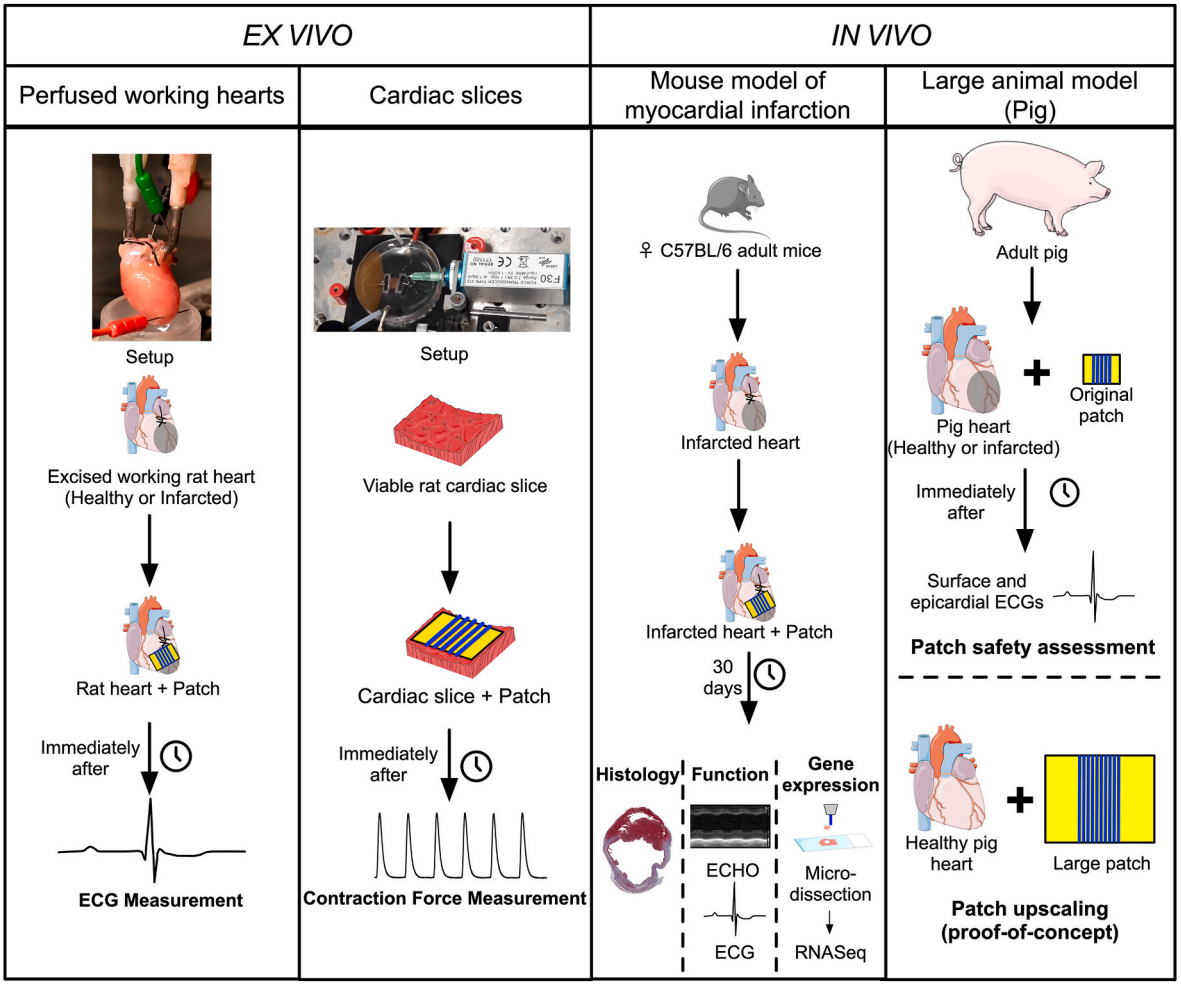

Fig. 1. Scheme summarizing the herein work. Description of the general approach of the *ex vivo* and *in vivo* experiments performed. Note: in all cases, the fibers are placed between the PCL nanofilm and the cardiac tissue; however, to simplify the visual representation of the fiber orientation, the schemes show the fibers as if they are on top of the nanofilm.

although they have been mainly tested for mechanical energy harvesting [25,26], recently their potential to support engineered heart tissues and subsequently improve remodeling and systolic function was shown in a rat model of MI [20]. Nevertheless, no study has yet evaluated the effect of the piezoelectric materials without seeded cells in the cardiac response to MI at the functional, molecular and electrophysiological levels [20].

In the current study, we have investigated the safety and the therapeutic efficacy of electroactive cardiac Piezo patches capable of generating electrical charge in response to deformation both *ex vivo* (isolated working heart and cardiac slices) and *in vivo* (mice subjected to MI as well as non-disease and MI-induced pigs) (Fig. 1). Importantly, Piezo patches are different from conductive patches since they generate electrical charge after mechanical deformation [27]. The cardiac Piezo patches tested were adopted from our previous study [24], with differences in the nanofilm composition (in this case without magnetic nanoparticles) and in the coating in the material. Piezo patches were composed of PCL nanofilms coated with aligned Piezo PVDF-TrFE nanofibers. Control (non-electroactive) patches were composed of PCL nanofilms coated with aligned PCL nanofibers. The PCL nanofilms in both types of patches were used in the patch construction has a mechanical support for the fibers (2–3 layers of fibers; to keep low the stiffness of the patch) and as a mean to have a flexible structure that would allow a better adjustment of the patches to the shape of the heart, thus allowing for the patches and, consequently the fibers, to move simultaneously with the heart movements. The functional impact of the cardiac patch in the MI mouse model was evaluated by transthoracic echocardiography (ECHO) and surface electrocardiography (ECG), and tissue recovery and molecular alterations were evaluated by histology and spatial transcriptomics, respectively. In the case of porcine model, the cardiac safety of the patch (in two different size formats) was assessed by epicardial ECGs. The results support the safety and efficacy of a new biomaterial-based approach for the treatment and electrocoupling recovery after MI, independently of their value to support cell-based applications.

2. Materials and methods

For detailed materials and methods please see Supporting Data.

2.1. Patch fabrication

Piezoelectric patches ("Piezo Patches") were prepared based on a previous protocol reported by us [24]. For most of the experiments reported in this study, a patch of 2 × 2.5 cm has been used except for some pig experiments in which a larger patch (7.5 × 6.0 cm) has been also prepared (see below). In brief, a sacrificial film was obtained by spin-coating a water-soluble polymer, poly(vinyl alcohol) (PVA) (1 % w/v, in water; Mw = 25.000, 88 % hydrolyzed; Polysciences, Inc.), over a silicon wafer (400 μm thick, 2 × 2.5 cm; Primewafers) at 4000 rpm for 20 s (Spincoat G3P- 8, Pi-Kem). Then, a poly(caprolactone) (PCL) suspension (20 mg/mL in chloroform; Mw = 80.000, Sigma) was spin-coated, with the same parameters, over the PVA layer. Aligned piezoelectric fibers were obtained by electrospinning (13 kV; tip to collector distance: 12 cm; injection rate: 2.5 mL/h; relative humidity: 40–50 %; room temperature; collector's rotation speed: 2.000 rpm; collection time: 4 min) a suspension of PVDF-TrFE (20 % w/v, in butanone; PVDF:TrFE (70:30) w/w; Solvay) over the PCL film. As for the control, non-electroactive patches ("PCL Patches") were formed in an identical manner as the Piezo Patches, except that aligned PCL fibers were deposited. These PCL fibers were obtained by electrospinning a PCL suspension (25 % w/v in formic acid/acetic acid (60/40)) with the same parameters as the PVDF-TrFE fibers, except for voltage that was at 23 kV. Upon immersion in an aqueous solution, the PVA sacrificial layer is dissolved, allowing one to completely detach and obtain free-floating PCL or Piezo patches.

For some of the pig heart experiments, larger patches were produced with, consequently, slight alterations in the fabrication procedure. First, PVA and PCL layers were subsequently spin-coated (2000 rpm for 20 s) over larger silicon wafers (400 μm thick, 7.5 × 6.0 cm, Primewafers). Regarding electrospinning, a larger rotating collector was designed and produced to fit the larger silicon wafers. The electrospinning parameters were the same as with the original small patches, except that the deposition time was prolonged from 4 min to 30 min.

2.2. Patch mechanical testing

Mechanical properties were evaluated by measuring the strain obtained in response to unidirectional stress applied to the samples. An INSTRON 5965 Mechanical Testing System was used, equipped with a ±10 N load cell. Traction tests were performed on seven samples for each experimental condition. All specimens were pulled at a constant speed of 5 mm/min, until reaching sample failure. Data were recorded at a frequency of 100 Hz. The stress was calculated as the ratio between the load and the cross-section area of a tensile specimen, while the strain was calculated as the ratio between its extension and its initial length. The Young's modulus for each tested sample was extracted from its stress/strain curve, as well as the elongation at break and the ultimate stress.

2.3. Patch electromechanical characterization

The electromechanical stimulation of the patches was performed using a linear stage (VT-80 Linear Stage, PI), applying a cyclic mechanical deformation of 10 % of their initial length, at a frequency of 1 Hz (Movie S1). Two electrodes made of adhesive copper (width: 1 cm, length: 3 cm) were deposited in the opposite planar faces of polyethylene terephthalate (PET) film (width: 1.5 cm, length: 3 cm), featured by a thickness of 28 μm. Before the measurements, the patch (width: 1.5 cm, length: 1.5 cm) was collected from water by a planar PET film, and consequently the opposite PET film was stuck to the patch/PET bilayer. The application of the displacement was parallel to the fiber orientation. To verify the piezoelectric behavior of the nanocomposite membranes, signals were also acquired by inverting the poles of acquisition. The electrical response of each patch was analyzed using an oscilloscope (PicoScope 2000 Series, Pico Technology), and signals were processed in Matlab (2022a). The signal acquisition was performed at room temperature and within an incubator at 37 °C (model 711/ct, Elettrofor). Three patches were analyzed for each condition.

Supplementary data related to this article can be found online at https://doi.org/10.1016/j.mtbio.2025.101742

Movie S1. Electromechanically-controlled patch deformation system.
Movie S2. Setup for *ex vivo* working heart.
Movie S3. *In vivo* patch implantation.
Movie S4. *In vivo* induction of myocardial infarction.
Movie S5. Piezo patch implanted in beating pig heart.
Movie S6. Large Piezo patch implanted in beating pig heart.

The piezoelectric characterization of the piezo patch was further supported using computational FE simulations. The FE model, built using COMSOL Multiphysics v6.0, replicated the bending observed in the experimental setup described above. The model included the piezo patch (thickness and Young's modulus detailed in Section 2.1) placed between two copper electrodes (thickness: 400 μm; Young's modulus:

Table 1
Material data input for FE simulation.

	Copper Electrodes	Piezo Patch
Thickness [μm]	400	1.25
Young's Modulus [MPa]	130e3	7.4
Coupling coefficients [pm/V]	/	d_{33}: 14.7; d_{31}: 12.74

130 GPa). All materials were considered linear and isotropic and the piezoelectric coupling coefficients measured experimentally (Supporting Data, section 2.3) and reported in Section 2.1 (d_{33}: 14.7 p.m./V, and d_{31}: 12.74 p.m./V). The material data are collected in Table 1.

A horizontal displacement equal to 10 % was applied to the extremities, with the aim to replicate the horizontal movement of the linear stage (Fig. S4A). The bottom copper electrode was set as the ground (zero electrical potential), while the top electrode served as the terminal (where the final electrical potential was computed). As the mechanical boundary conditions were imposed in the extremities, the analysis was split in two sequential studies: i) the Linear Buckling Analysis to find the mode shape, and ii) the Post-buckling Analysis to compute the other parameters (displacement, stress and thus electrical potential). The system of partial differential equations was solved through the Multiphysics option 'Piezoelectric Effect' present in COMSOL Multiphysics v6.0. The stability of the results was ensured through a mesh convergence analysis.

2.4. Scanning electron microscopy (SEM) imaging of the patches

Before imaging, all samples were coated with a thin gold layer through a sputter machine (Q150R ES, Quorum Technologies) equipped with a gold target, by applying a current of 25 mA for 90 s. Then, SEM images were acquired through a scanning electron microscope (SEM, EVO MA15, Zeiss Instrument). SEM scans were performed by setting a beam voltage of 20 kV, a probe current of 150 pA and different magnifications (3000 × , 6500 × and 15000 ×). At least six images were taken per each sample and each magnification.

2.5. Animal experimentation

The mice experiments were performed at i3S (Instituto de Investigação e Inovação em Saúde) (Porto, Portugal). All experimental protocols were authorized by the internal IACUC and the national veterinary agency (Ref: 0421/2017). Adult female C57BL/6 mice aged 8–10 weeks were used in these experiments (Sham: 6 animals; MI-only: 11 animals; PCL: 9 animals; Piezo: 9 animals). Female mice were chosen for these experiments because they have better survival after myocardial infarction, less incidence of cardiac rupture, improved LV function and cardiac remodeling [28–30]. Humane endpoints were considered according to OECD Guidance Document on the Recognition, Assessment, and Use of Clinical Signs as Humane End points for Experimental Animals Used in Safety Evaluation (2000). The 3Rs principles (Reduction, Replacement and Refinement) were applied. All the aforementioned procedures are in conformity with the European Directive 2010/63/EU.

Animal experimentation regarding *ex vivo* rat myocardial slices was performed at the National Heart & Lung Institute, Imperial College (London, UK). Adult male Sprague Dawley rats were used (3 animals used in total). These experiments were compliant with Imperial College and UK national regulations. The procedures were performed under license by the UK Home Office, in accordance with the United Kingdom Animals (Scientific Procedures) Act 1986. The 3Rs principles were applied.

The *ex vivo* rat heart procedures were performed at the Faculty of Medicine of the University of Porto (Porto, Portugal) and they were authorized by the internal IACUC and the national veterinary agency. The 3Rs principles were applied. A total of 4 rats were used for these experiments.

The pig experiments were performed at the Faculty of Medicine of the University of Porto (Porto, Portugal) and were authorized by the internal IACUC and the national veterinary agency (DGAV 2021-07-30 011706). All procedures were performed by researchers and veterinarians authorized to perform animal research. The 3Rs principles were applied. Pigs used for patch analysis were reused from ongoing protocols. A total of 6 animals were used: 4 pigs were used in a normal health state, while two were subjected to the induction of ischemia.

2.6. Ex vivo healthy/infarcted rat working-heart setup

Isolated rat hearts were set up in a working heart preparation as previously described [31]. Heart and lungs were quickly excised *en bloc* under sevoflurane anesthesia and placed in ice cold heparinized modified Krebs-Henseleit (KH) solution supplemented with 30 mM BDM. The lung hila were ligated with surgical titanium clips and the lobes excised. The aorta was quickly dissected and mounted onto a cannula dripping KH solution at 37 °C and equilibrated with a mixture of 95 % O_2 and 5 % CO_2. Aortic (and therefore coronary) pressure was then set at constant 80 mmHg by adjusting the height of an open perfusate reservoir and the hearts spontaneously start beating, stabilizing at an intrinsic rate of 220–280 bpm. The left atrium is then cannulated and a fixed preload of 5–10 mmHg is set to establish an ejecting preparation. In this working heart model, the perfusate is pumped from the left ventricle anterogradely onto the aorta, as the 80 mmHg column becomes the afterload. A single intracardiac ECG lead was obtained with negative and positive needle electrodes placed in the right atrium and apex, respectively. After a period of stabilization, the epicardial surface of the LV was sequentially covered with the Piezo or PCL patches. Both patches were adhered to the left ventricle surface with fibrin glue, using a biopsy punch as a support. The same procedure was repeated after inducing ischemia by left anterior descending artery ligation (LAD) for 20 min. ECG data was recorded with LabChart software (AD Instruments, New Zealand).

2.7. Preparation of rat myocardial slices

Rat myocardial slices were prepared as described in previous reports [32,33]. Briefly, after sacrificing adult male Sprague Dawley rats, hearts were excised and placed in warm heparinized Tyrode's solution supplemented with 30 mM 2,3 butanedione monoxime (BDM, Acros Organics) to remove blood from the LV (5–10 s at 37 °C), then immediately placed in cold Tyrode's solution supplemented with BDM (at 4 °C). Afterwards, the LV was isolated and then flattened by means of an incision on the interventricular septum. Following the attachment of the tissue on a specimen holder, it was placed in a bath (composed of oxygenated Tyrode's solution supplemented with BDM, at 4 °C) of a high-precision vibratome (7000 smz-2, Campden Instruments). Finally, the LV was sliced longitudinally to the myocardial fiber orientation, from the endocardium to the epicardium (ceramic blade; vibration: 80 Hz; amplitude: 2 mm; Z-axis error: <1.0 μm). Slices were maintained immersed in oxygenated cold Tyrode's solution supplemented with BDM (at 4 °C) until contractility measurements were performed.

2.8. Rat myocardial slice contractility measurements

To assess myocardial slice contractility, slices were trimmed so that only the areas where the myofibrils were the most aligned would be used (approximate average dimensions after trimming – length: 7 mm; width: 7 mm; thickness: 300 μm) [32,33]. Next, PCL or Piezo patches (49 mm^2) were detached from the silicon substrates while in Tyrode's solution supplemented with BDM and then glued (with Histoacryl surgical glue; Braun, cat. no. 1050052) in two polytetrafluoroethylene (PTFE) rings (on the patch opposite sides) which were, in turn, glued to the opposite ends of the trimmed cardiac slices, perpendicularly to the myofibrils. Thus, patches were applied in close physical contact with the slices, as such the polymeric fibers were aligned with the myofibrils. The slice + patch + rings construct was then attached to a force transducer (Harvard Apparatus) and immersed in a bath of Tyrode's solution without BDM. The bath and the slices were electrical field-stimulated (1 Hz; ~20 V). The force transducer includes a system by which the displacement (d) caused by the slice contraction is directly measured, which can be converted to units of force (F) through a constant specific for the equipment: F (mN) = 0.81 × d (μm). Furthermore, F was normalized to the cross-sectional area of the slices to obtain slice contractility.

Myocardial slices were stretched unidirectionally, at different extents, simulating different cardiac preloads, expressed as sarcomere length (SL), namely: SL = 1.8 μm (initial measurement); SL = 2.2 μm; and SL = 2.4 μm. SL was indirectly determined for each cardiac slice by means of a previously determined correlation between SL and % of stretch (distance between ends of stretched myocardial slice/resting length of myocardial slice × 100). It was determined that SL = 1.8 μm, SL = 2.2 μm and SL = 2.4 μm corresponds to a stretch of 0 %, 17 % and 30 %, respectively (data not shown). For each preload condition, contractility was acquired for 2 min, and then the contractility amplitude of three peaks from a constant, stable portion of the trace was measured. Data were recorded using AxoScope software and peak amplitude analyses were conducted using Clampfit software (Molecular Devices, USA).

2.9. In vivo induction of myocardial infarction and patch implantation

MI was experimentally induced *in vivo* by means of permanent ligation of the LAD coronary artery, as previously described [34], with slight alterations. Briefly, mice were submitted to a left thoracotomy on the third intercostal space, exposing the heart. The pericardial sac was gently disrupted and the first portion of the LAD artery was ligated with a non-absorbable 7/0 suture (Silkam; B. Braun), inducing MI. Patches were immersed beforehand in a 1 % penicillin/streptomycin (P/S) saline solution (100 U/mL penicillin and 100 μg/mL streptomycin, Labclinics) to allow their detachment from the silicon substrates. After MI induction, the patches were placed on a biopsy punch (Ø – 4.0 mm; BPP-40F; kai medical) and then covered with a two-component porcine fibrin glue (fibrinogen concentrate, 49–55 mg/mL: thrombin, 18–20 NIH units/mL, 20 μL:1 μL; F007; zedira GmbH). Subsequently, patches were applied by pressing the patches (side containing fibers), for 20 s, against the epicardium of the exposed infarcted myocardium. The patches were applied in an oblique manner, so that most of the polymeric fibers would become parallel to the myocardial fibers, as they are itself oriented obliquely [35]. Thereafter, the biopsy punch was detached from the patch, and the unattached borders of the latter were removed by fine scissors. Finally, intercostal and skin incisions were closed by an absorbable 6.0 suture (Safil, B. Braun) and surgical staples, respectively. Analgesia and fluid therapy treatments were performed every 12 h up to 72 h after surgery or until full recovery.

2.10. In vivo evaluation of cardiac function: echocardiography and electrocardiography

Animals at 30 days post-MI were subjected to transthoracic echocardiography using the VEVO® 2100 system (Visual Sonics) coupled to a 40-MHz probe (see Supporting Data for detailed information).

Two-dimensional (2D) images were acquired of both short-axis (SAX) and parasternal long-axis (PSLAX) views. In SAX view, these were required to properly position the Motion-mode (M-mode) cursor so that the dimensions of the LV cavity and LV walls (at systole and diastole) could be measured. PSLAX view images allowed to determine cardiac output (CO), by resorting to the Pulsed Wave Doppler (PW) Doppler mode. The LV internal diameter during diastole (LVIDd) and systole (LVIDs), obtained in SAX view in M-mode, were used to calculate fractional shortening (FS) and ejection fraction (EF). Furthermore, LVIDd, LV posterior wall thickness (LVPW), and LV anterior wall thickness (LVAW) (measured in SAX view) were used to estimate LV mass. The ascending aorta diameter, or LV outflow tract diameter (LVOT), and the velocity-time integral of the aortic flow (VTI) (measured in PW Doppler mode), allowed the calculation of stroke volume (SV), that, in turn, in combination with the HR, was required to determine the CO: CO=SV × HR. Epicardial areas in systole and diastole (EPIareas and EPIaread, respectively), and endocardial areas in systole and diastole (ENDOareas and ENDOaread) were measured in the SAX view images, being the latter two used to calculate endocardial fractional area change (see Supporting Information for detailed information and formulas).

Electrophysiological parameters were assessed at 30 days post-MI by means of surface ECGs. ECG signals were obtained using a data acquisition hardware (PowerLab 8/35; ADInstruments) coupled to a signal amplifier (Animal Bio Amp; ADInstruments) and ECG electrodes, with the support of the LabChart 8 software (ADInstruments). The equivalent of a lead II configuration was used to obtain the ECG signals.

2.11. Infarcted mouse cardiac tissue harvesting, processing and staining

At 30 days after surgery, animals were deeply anesthetized and after 4 M potassium chloride (Sigma-Aldrich) injection, diastole-arrested hearts were harvested and washed in PBS. For the means of histological characterization, infarct size quantification and immunohistochemistry, hearts were fixed in 10 % (v/v) neutral buffered formalin (Prolabo; VWR International) for approximately 16 h at RT. Hearts were then processed for paraffin embedding. Conversely, the hearts used for RNA extraction from microdissected tissue were snap frozen in dry ice and embedded in Optimal Cutting Temperature compound (OCT) immediately after harvesting, without fixation, to better preserve RNA integrity.

Paraffin-embedded hearts were sectioned transversally (microtome RM2255; Leica) from the apex to the base. In order to achieve a representative sampling of the LV, 3 μm-thick sections were obtained from equidistant regions (300 μm) of the LV. To assess the presence of the patches at early timepoints and to perform morphometric analysis/infarct size quantification, the paraffin sections were stained with Hematoxylin-Eosin (HE), modified Masson's Trichrome (MT) or Picrosirius Red (PSR), (see Supporting Data for detailed information).

Relatively to the OCT-embedded hearts, they were cryosectioned (15 μm-thick sections from equidistant regions, 50 μm), into polyethylene naphthalate (PEN)-membrane microscope slides (MembraneSlide 1.0 PEN, Carl Zeiss), which were pre-treated with heat (180 °C for 4 h) to inactivate RNAses, and UV radiation (254 nm for 30 min) to increase hydrophilicity. The sections were either immediately stained or stored at −80 °C in a dry environment.

For histological identification of the regions of interest for microdissection, while preserving RNA integrity, the aforementioned cryosections were stained with an altered quick HE protocol performed with fresh, pre-cooled solutions (see Supporting Information for detailed information). After leaving sections to air-dry for 5 min, the stained sections were immediately microdissected or stored at −80 °C.

2.12. Measurement of myocardial infarction size and morphometric analysis

To determine infarction, deposited collagen, which becomes stained blue when subjected to Masson's Trichrome staining, was used to define the LV scarred region. Stereomicroscope-acquired low magnification images of the MT-stained histological section were analyzed using the semi-automated software MIQuant [36]. This software determines the percentage of ischemic LV wall by two distinct methods: area measurement [34,37] and midline length [37]. Morphometric analysis was executed by using the Image J software (NIH). LV wall thickness was determined on regions that exhibited collagen deposition in 50 % or more of the wall and calculated as the average of the distance across the wall of five equidistant points of the ischemic wall. LV dilation was assessed by the lumen-area percentage, *i.e.* the ratio between the lumen area delimited by the endocardium and the total LV area. The cross-sectional area of the LV cardiomyocytes on the myocardial region far from the Patch was measured in at least 25 cardiomyocytes per section (at least 4 sections were analyzed per heart).

2.13. Microdissected mouse myocardial tissue spatial analysis

2.13.1. Laser capture microdissection (LCM)

LCM of HE-stained mouse myocardial tissue cryosections adhered to the PEN MembraneSlides was executed using a Zeiss PALM MicroBeam system (Carl Zeiss) coupled to a Zeiss Observer Z1 microscope (Carl Zeiss) with a 5x FLUAR objective (Carl Zeiss). In brief, five 1x10^5 μm^2-microdissection elements (total of 5 × 10^5 μm^2, approximately) were cut from each section replicate of each region of interest, i.e. cardiomyocytes near patch (PCL-Infarcted and Piezo-Infarcted), cardiomyocytes from the LV but far from patch (PCL-Remote and Piezo-Remote). These elements were then catapulted and captured into the lid of AdhesiveCap opaque tubes (415190-9201-000, Carl Zeiss) for further RNA isolation.

2.13.2. RNA extraction

Total RNA was extracted from the microdissected myocardial tissue elements. Microdissected myocardial tissue elements were first lysed with RLT Buffer (30 min), from RNeasy® Micro Kit (74004, Qiagen), containing 1 % of β-mercaptoethanol (M7522, Sigma) and then spun down (13.400 g, 5 min). Thereafter, lysates were processed with the RNeasy® Micro Kit to obtain the total RNA, according to the manufacturer's instructions. Briefly, the lysate in RLT buffer was first mixed to an equal volume of 70 % ethanol. This mixture was then transferred to a RNeasy MinElute spin column and centrifuged by 15 s at 8100 *g*. Afterwards, the spin column was washed with 700 μL of Buffer RW1 and centrifugation (15 s; 8100 *g*). Then, the spin column column was further washed with 500 μL of Buffer RPE under the same centrifugation conditions as the previous step. Thereafter, the spin columns were further washed with 80 % ethanol and centrifuged at 8100 *g* for 2 min. The columns were then dried by centrifuging them for 5 min at 14 000 *g*. Finally, the total RNA was eluted by centrifugation (1 min, 14 000 *g*) with 14 μL of RNAse-free water. The RNA samples were then sent to BGI Company Ltd (Hong Kong) were they were further processed and sequenced.

2.13.3. RNA quantification and quality assessment

RNA quantification and quality assessment was evaluated using an Agilent 2100 Bioanalyser equipment in combination with the RNA 6000 Pico Kit. Briefly, RNA was run in a gel in electropherograms and the intensity profile of the resulting bands was analyzed. The concentration and quality of the RNA were calculated based on the presence, intensity and ratio of intensities between the two expected bands that correspond to intact RNA of the ribosomal subunits 18S and 28S, as well as taking into account the present of extra bands between these two bands (which might signify degradation or presence of other contaminants). Through the analysis of the electropherograms of all the samples, a RNA integrity number (RIN) was automatically determined (1–10, being 10 the most intact RNA), which comprises a measure of RNA quality. A threshold of RIN $>$ 5.5 was defined for the samples to advance for sequencing.

2.13.4. Library construction and sequencing

For library construction and ribosomal RNA depletion, a NuGEN Trio kit (Tecan) was used. Briefly, the workflow starts with the synthesis of first strand cDNA via priming at the 3' end of RNA randomly throughout the transcriptome. Afterwards, second strand cDNA is synthesized and amplified with Single Primer Isothermal Amplification (SPIA), followed by end-repair to generate blunt ends, ligation of barcoded adaptors, and PCR amplification to produce the final library. The SPIA technology was combined with DimerFree adaptor ligation and AnyDeplete targeted transcript deletion that is workflow that is adequate for low input and poor-quality samples.

The library was sequenced was sequenced using PE100 (paired-ended 100-base pair) sequencing on a BGISEQ-500 system (BGI Ltd. Hong Kong). The BGISEQ-500 system features the combinatorial Probe-Anchor Synthesis (cPAS) and DNA Nanoballs (DNB™) technologies [38]. cPAS chemistry involves the incorporation of a fluorescent probe to a DNA anchor on the DNBs, followed by high-resolution digital imaging. The DNB™-based technology is further described in the literature [38]. Briefly, using a controlled synchronized synthesis, hundreds of tandem copies of the sequencing substrates in palindrome-promoted coils of single-stranded DNA (the DNBs). DNBs are adsorbed onto photolithographically etched silicon substrates with grid-patterned arrays of ~300-nm spots for DNB binding. cPAS chemistry was then used to independently read up to 10 bases adjacent to each of eight anchor sites resulting in a total of 31- to 35-base mate-paired reads (62–70 bases per DNB) [38].

2.13.5. Bioinformatic data analysis

Approximately 50 million of 100-bp paired-end reads were yielded for each sample. Sample read quality was determined using FASTQC. Then, using Trimmomatic [39] (a line of code customizable to the adaptors used in the sequencing system) the low-quality sequences (i.e. with the Phred score $<$30) were dropped and adapter sequences were trimmed. The resulting reads were aligned to the reference mouse genome (GCRm38.p6/mm10) using HISAT2 [40]. Gene count files were performed in featureCounts using Galaxy online software [41]. Differentially expressed gene (DEG) analysis was performed with DESeq2 in Galaxy (ver. 2.11.40.6), using DEG selection criteria of ($\log_2$(Fold Change)) $>$ 2 or $<$ −2 and FDR $<$0.05. DESeq2 was used instead of edgeR because the former is more appropriate for assays with a low number of samples since it normalizes the data using median, while edgeR uses the mean. In addition, DESeq2 filters low counts while edgeR does not.

Gene ontology (GO) analysis was performed by resorting to *Enrichr* web tool (https://maayanlab.cloud/Enrichr/) and the gene-set library named *GO Biological Process 2021* [42,43]. This is a curated collection of biological process terms from the Gene Ontology (GO) database, updated in 2021. These terms categorize gene functions based on biological processes. The top 5 of the Biological Processes were sorted based on the highest $\log_{10}$(1/adjusted p-value) values. Principal coordinate analysis of all samples was performed using the PCA plot function of ggplot2 in Galaxy (ver. 2.2.1.). Expression heatmaps were assembled using Heatmapper online software [44], using complete clustering and Kendall's Tau distance measuring method. Volcano plots were performed using *Volcano plot* function in Galaxy (ver. 0.0.2).

2.14. In vivo patch implantation in healthy or infarcted pig heart models and ECG measurements

Experiments were performed in Landrace × Pietrain breed, using male animals weighing 30–60 kg, from an authorized breeder. All terminal experimental protocols in the facility culminated in sample collection after medial sternotomy under anesthesia and analgesia. Prior to sample collection, the patches were tested by applying epicardially using fibrin glue. A total of six pigs were used. Five were used for the epicardial ECG acquisition with small patch implantation (three were non-disease and two underwent MI induction). One non-disease pig was used for the implantation of a large patch (proof of concept experiment).

For MI induction, ischemia-reperfusion injury was induced percutaneously using a coronary angioplasty balloon, as previously described [45]. After canulating the left coronary artery with a JL3 guide catheter, a 0.014 in guidewire was used to selectively engage the left descending artery (LAD). A rapid exchange coronary angioplasty balloon (2.5 mm in diameter) was placed in the LAD after the first diagonal branch, and inflated for 120 min, followed by reperfusion and animal recovery.

For epicardial signal acquisition, epicardial pacing wires were sutured in parallel to pieces of PTFE grafts (0.5 × 0.5 cm). The loose ends of the wires were connected to a PowerLab system (ADinstruments) through BNC to Alligator Clips cables. Signals were acquired, recorded and analyzed offline using LabChart 8 (ADinstruments).

2.15. General statistical analysis

Values presented in text and figures are mean ± standard error of mean (SEM). Data statistical analysis was performed using GraphPad Prism version 7.00 for Mac (GraphPad Software, La Jolla California, USA, www.graphpad.com). Outliers were excluded from the statistical analysis. The method used to identify outliers was the ROUT method [46] (Q = 10 %). Shapiro-Wilk's test was used to evaluate if the data displayed a normal distribution. If so, the homoscedasticity of the data was tested by F test. These results defined the statistical test(s) used

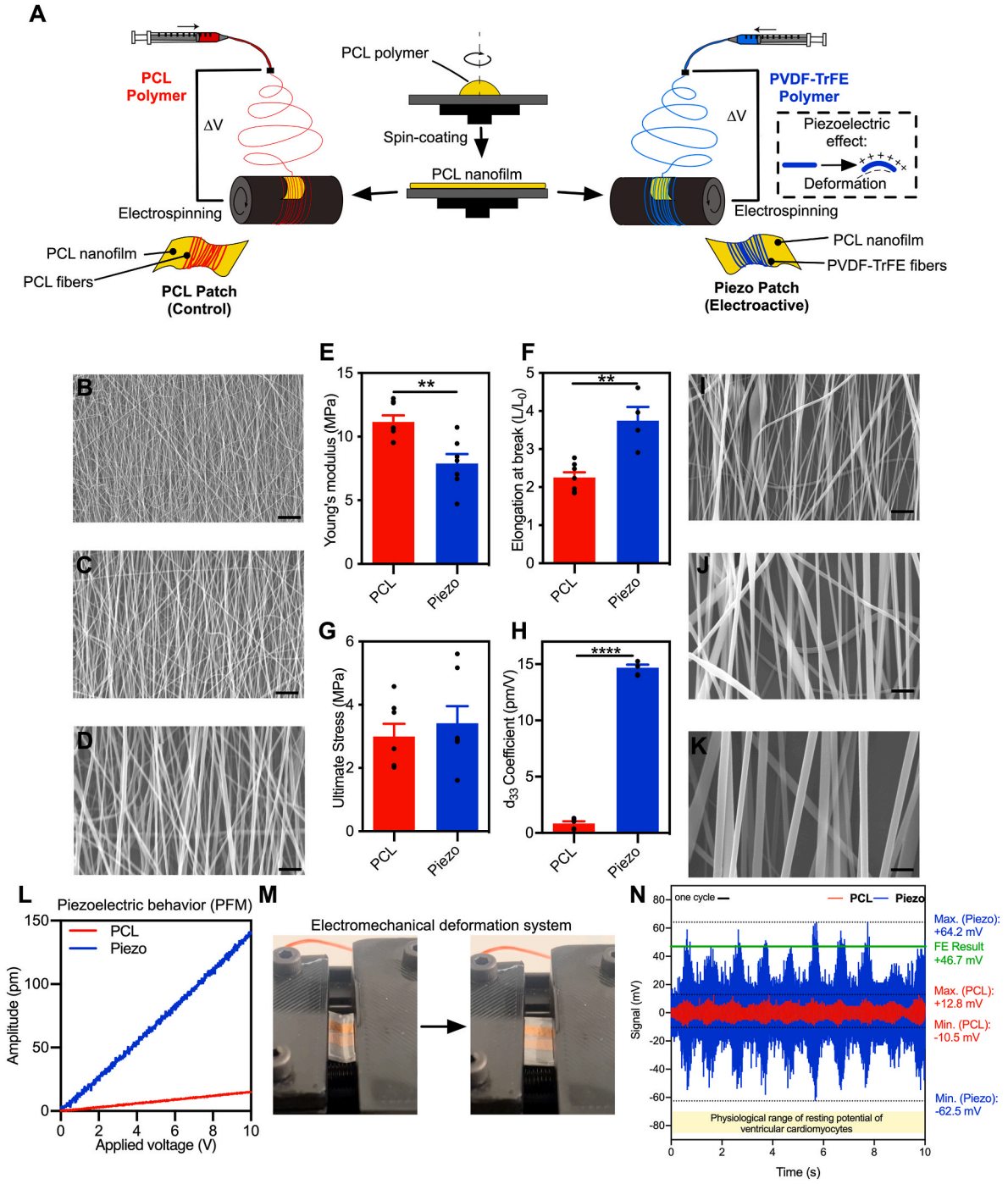

Fig. 2. Patches Production and Characterization. (A) Process of fabrication of PCL and Piezo patches using spin-coating and electrospinning. (B-D, I-K) Representative SEM images of PCL patch (B–D) and Piezo patch (I–K) fibers. Scale bars: B and I – 10 μm, C and J – 5 μm, D and K – 2 μm. (E–G) Mechanical characterization of the patches by Young's Modulus (E), Elongation at break (F) and Ultimate Stress (G). (PCL patch: n = 8 for E and F, n = 7 for G; Piezo patch: n = 7 for E and G, n = 4 for F). (H) Comparison of the piezoelectric coefficient (d_{33} coefficient) between both groups. (n = 3 specimens per group). (L) Piezoelectric behaviour shown as the amplitude signal detected by varying the voltage applied with the tip. (M) Representative image of one cycle of mechanical bending (left: bent position; right: unbent position) resorting to a controlled electromechanical system to impose the deformations. (N) Voltage signals measured upon several bending cycles (1 Hz) of PCL and Piezo patches. Maximum and minimum voltages detected from each patch group are denoted in the right side. FE result is reported in green. All values presented as mean ± SEM. **p < 0.01; ****p < 0.0001. One outlier was excluded in F (PCL group). Statistical analysis: Unpaired *t*-test (E–H). (For interpretation of the references to colour in this figure legend, the reader is referred to the Web version of this article.)

further. Normal distributed and homoscedastic data were tested with parametric tests (independent samples *t*-test). Non-normal distributed and/or heteroscedastic data were tested with non-parametric tests (Mann-Whitney *U* Test). The statistical significance level chosen for all statistical test was $p < 0.05$.

3. Results and discussion

3.1. Generation of electroactive and non-electroactive patches

We designed flexible polymeric PCL nanofilms (average thickness: 37 ± 6 nm) coated with aligned Piezo PVDF-TrFE nanofibers (fiber Ø = 741 ± 28 nm, average ± SEM, n = 6) (Piezo patches), according to a methodology previously reported by us (Figure S1 and Fig. 2A; 2I-2K) [24]. Using a similar approach, PCL nanofilms were coated with aligned PCL nanofibers (fiber Ø = 235 ± 7 nm, average ± SEM, n = 6) (PCL patches) (Fig. 2B–D) and used as a control for the remaining experiments. The estimated total thickness of the patches (*i.e.* the thickness of the PCL nanofilm in combination with the layer composed of multiple fibers) was 1.25 μm for the Piezo patches and 0.75 μm for the PCL patches (Fig. S1). Piezo and PCL patches stiffness measured by tensile tests, showed an elastic modulus of 7.9 ± 0.7 MPa (average ± SEM, n = 7) and 11.2 ± 0.5 MPa (average ± SEM, n = 8), respectively (Fig. 2E–G). Although these Young's moduli are one to two orders of magnitude over the mouse myocardial scar tissue (0.1–0.8 MPa) [47], they are in the same range as other reported cardiac patches (e.g. 6.7 ± 1.1 MPa) [6]. Moreover, PFM analysis showed that Piezo patches had higher piezoelectric coefficient (d_{33}) (d_{33} = 14.7 ± 0.4 p.m./V for the Piezo patches versus d_{33} = 0.9 ± 0.4 p.m./V for the PCL patches) than PCL patches, thus, exhibiting piezoelectric properties (Fig. 2H and S2).

PFM analysis also evidenced that Piezo patches exhibited a piezoelectric inverse effect, as the Piezo PVDF-TrFE nanofibers suffered a considerably steeper increase in displacement with an increasing applied voltage to the PFM tip, when compared with the PCL controls (Fig. 2L). To evaluate the piezoelectric properties at macroscale level, an electrode-equipped electromechanically controlled platform was developed for repeated patch deformation (Fig. 2M; Fig. S3; Movie S1). Voltage was measured in the patches upon cyclic patch deformations in a linear stage (Fig. 2M and N), with a deformation of 10 % of the initial patch length, and evaluating the influence of the temperature by comparing the response at room temperature and at 37 °C, the normal physiological temperature (Fig. S3). Results showed that PCL patches were not responsive to the mechanical deformation, while the Piezo patch could generate, in average, an electrical signal with peaks of almost 50 mV and a maximum of, approximately, 60 mV demonstrating its piezoelectric nature (Fig. 2N). Of note, the environment temperature had a negligible effect (average value 38.6 mV and 40.5 mV at room temperature and 37 °C, respectively, n = 3) (Fig. S3), in agreement with the literature [48]. Interestingly, this electrical signal generation was synchronized with the exerted strain (Fig. S3).

The piezoelectrical characterization of the patch was further described by computational finite element (FE) simulations, whose results are presented in Fig. S4. The simulations replicated the experimental conditions in terms of materials and boundary constraints, including the PVDF-TrFE patch placed between two copper electrodes (Fig. S4A). The electrical potential obtained from the FE simulation was 310 mV, resulting from the bending of the copper electrodes (Fig. S4B). This potential was highest at the patch and decreased toward the top and bottom surfaces due to the copper's thickness (Fig. S4B, zoom). The electrical potential at the copper surface was 46 mV, as shown in Fig. S4C. Experimentally, the measured values were slightly lower (average value 40.5 mV), likely due to losses and noise not accounted for in the FE simulations. The comparison between FE result and experimental measurements in terms of electrical potential obtained from the film bending is reported in Fig. 2N. The stability and accuracy of the solution of the electrical potential was ensured by the mesh convergence analysis, whose result is presented in the Fig. S4D.

The peaks of the electrical potential are correlated to the stress distribution, whose average value on the piezo patch is 2.78 MPa (Fig. S4E).

Considering that the resting membrane potential of ventricular cardiomyocytes is approximately −85 mV and that their respective threshold potential is around −70 mV [8,49,50], theoretically, the peaks at 50 mV generated in an *in vivo* setting by the Piezo patches would be able to increase cardiomyocyte potential above the threshold and generate action potentials. In fact, in a previous study, *in vitro* cardiomyocytes were shown to up-regulate the expression of *Adss1*, a gene previously shown to be activated upon the electrical pacing [51], in response to scaffolds similar to the Piezo patches [24].

3.2. Ex vivo effect of Piezo patches on non-disease and ischemic rat hearts

To investigate the impact of Piezo patches on electrophysiology and contractile function, Piezo patches were applied *ex vivo* to ejecting rat hearts (Movie S2). PCL patches were used as control. Of note, the current patch is thinner than previously reported cardiac patches (19 μm - Mawad et al. [6]; 29 μm - Kapnisi et al. [7], 100 μm - Montgomery et al. [5]). All patches maintained conformal contact, without physical rupture, for the duration of the experiments. ECG measurements were then performed in hearts implanted with Piezo or PCL patches and compared to the same heart before patch implantation (No Patch) (Fig. 3A and B). Neither of the patches caused any changes in the ECG morphology (Fig. 3B) suggesting that PCL and Piezo patches did not disrupt the propagation of the cardiac action potential of non-disease hearts.

We then evaluated whether the patches would interfere with cardiac electrophysiological function after MI. In the same *ex vivo* setting, hearts were subjected to left anterior descending (LAD) coronary artery ligation, patches were implanted and ECG measurements were performed. As expected [52,53], ischemic hearts showed distinctive alterations in the repolarization phase (Fig. 3C). Importantly, as with the non-disease hearts, the implantation of either PCL or Piezo Patches did not show relevant changes in the ECG morphology (Fig. 3C).

Overall, our results show that the Piezo patches had no detrimental impact on cardiac electrophysiological properties using an isolated working rat heart model. Importantly, no arrhythmias were observed upon patch application, endorsing their safety *in vivo*. This is an important aspect for the future therapeutic application of these patches. Piezoelectric devices to harvest energy from cardiac motion have been reported previously [25] but their effect in the electrophysiology of the heart had not been investigated.

3.3. Effect of piezo patches on healthy rat cardiac slices

To further characterize the impact of Piezo patches in cardiac tissue function, we assessed the effect of cardiac patches on myocardial contractility. For this purpose, ultrathin slices (300–400 μm) of living adult ventricular myocardium were used. These slices represent a relevant model since they allow the direct measurement of the myocardial contractility, they retain the native multicellularity, architecture, and physiology of the cardiac tissue, while their small thickness ensures adequate oxygen and metabolic substrate availability through diffusion *in vitro* [32]. Piezo and control PCL patches (49 mm^2) were applied in close contact with healthy rat cardiac slices (Fig. 3D–F). In this setting, patches deform alongside with the contraction/relaxation motion of the cardiac slice, generating electric charges locally; hence, one can assess the effect of this piezoelectric activity on the contractility of the myocardium. The combination of slice and patches was unidirectionally stretched, as a whole, with a force transducer-associated apparatus (Fig. 1; Fig. 3E and F) to different extents, corresponding to a sarcomere length (SL) of 1.8 μm, 2.2 μm and 2.4 μm on the slice. Then, the contraction force was measured during electrical field cyclic stimulation

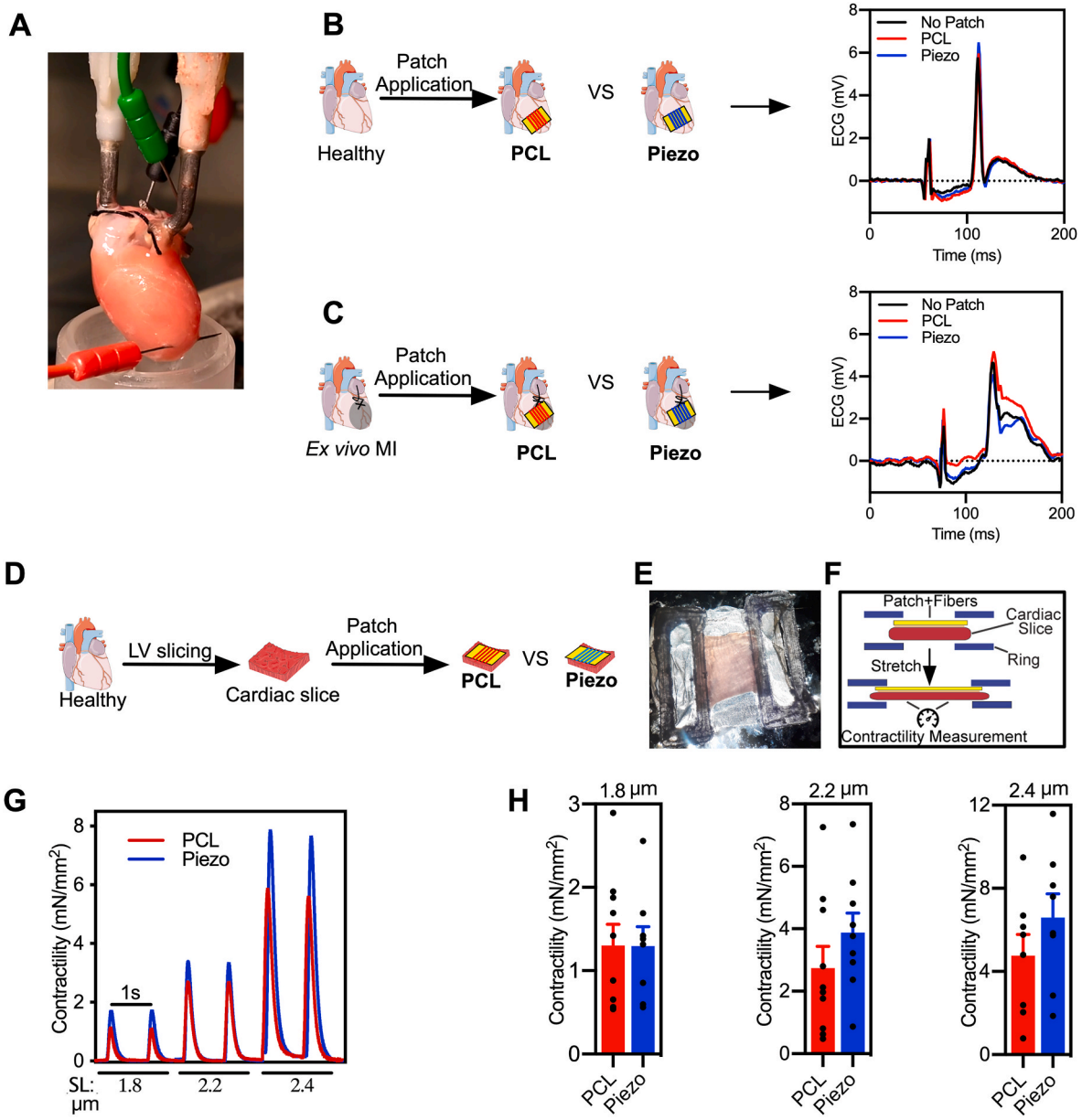

Fig. 3. *Ex vivo* evaluation of Piezo Patch Tissue Function. (A to C) Electrophysiological effect of the Piezo patches on perfused working whole rat hearts. A particular experimental setup for perfusion and ECG acquisition (A) was used to measure ECG signals (B and C). (B and C) Experimental design and representative ECG traces (one cycle) of healthy (B) and MI (C) hearts before and after applying Piezo or PCL patches. (n = 2 animals for all conditions). (D to H) Contractility effect of the Piezo patches on viable rat cardiac slices. The PCL or Piezo patches were glued to the cardiac slices (D), along with plastic rings (E and F) then the system was extended as whole for contractility measurement (F). (G) Representative contractility traces comparing both PCL and Piezo patches, for three distinct sarcomeres lengths (SL). (H) Summary of contractility values comparing both groups (PCL: n = 10 for SL = 1.8 and SL = 2.2, n = 8 for SL = 2.4; Piezo: n = 9 for SL = 1.8 and SL = 2.2, n = 8 for SL = 2.4). All values are presented as mean ± SEM. *p < 0.05; ***p < 0.001. One outlier excluded in H (1.8 µm; Piezo group). Note: in all cases, the fibers are placed between the PCL nanofilm and the cardiac tissue however, to simplify the visual representation of the fiber orientation, some schemes (B,C and D) show the fibers as if they are on top of the nanofilm. Statistical analysis: Unpaired *t*-test (H).

(Fig. 3G and H). No statistically significant differences were detected between the PCL and Piezo patch groups (Fig. 3H and Figs. S5A–C). Moreover, with the 1.8 and 2.2 µm, although there is a tendency for the patch-containing slices to present decrease contractility when compared to the patch-free group, no statistically significant differences were detected. Relatively to the overload condition (SL = 2.4 µm), the PCL patch caused a significant reduction when compared to the patch-free group, however the Piezo group did not show such behavior, potentially due to a compensation by electrical charge stimulation.

These results suggest that the local electrical stimulation provided by the piezoelectric fibers does not preclude cardiac tissue contractility.

Altogether, our results importantly demonstrate that, under the tested conditions, both Piezo and PCL patches are functionally safe. Therefore, the Piezo patches constitute a promising platform for myocardial stimulation without interfering with cardiac electrophysiology nor contractility. These results compare favorably with respect to previous studies showing that auxetic conductive cardiac patches undesirably reduced the contractility of the myocardial tissue [7]. A limitation of the present study is that the piezoelectric nature of our patches requires deformation to generate an electric charge, which is incompatible with methods that require static conditions to quantify the propagation of action potential at the tissue/cellular level such as

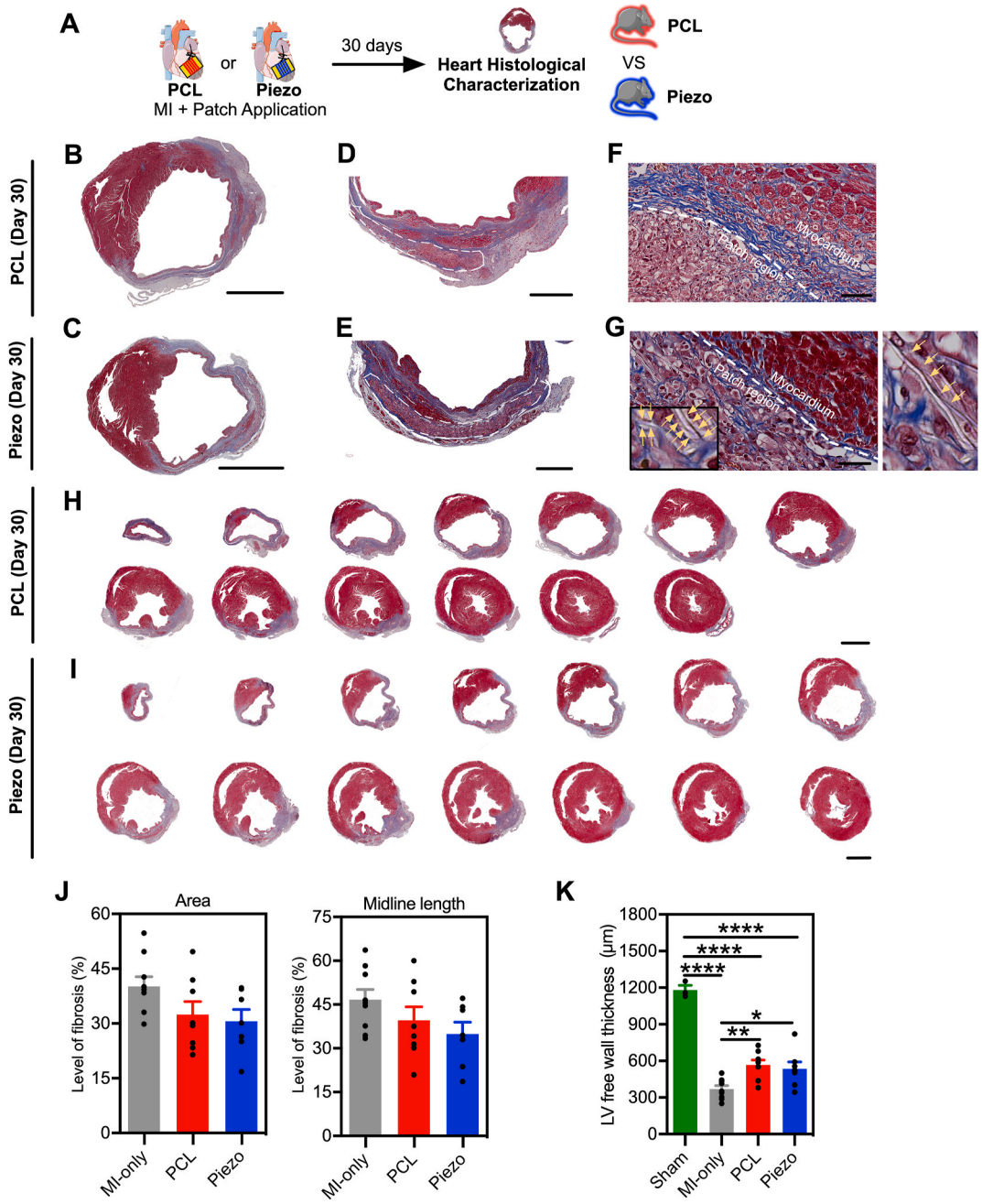

Fig. 4. *In vivo* effect of piezo patch on cardiac tissue remodeling by histological characterization. (A) Experimental Procedure and timeline leading to the histological analysis. (B to G) High-resolution whole-section images of representative Masson's Trichrome stained sections of hearts, at 30 dpmi, of both PCL (B, D and F) and Piezo (C, E and G) groups. Polymeric fibers are visible in the Piezo group (G, inset, yellow arrows placed along one; image at the right side contains another example of piezoelectric fibre). Scale bars: B and C – 2 mm, D and E – 500 µm, F and G – 50 µm; G inset: 3x magnification. (H and I) Representative Masson's Trichrome-stained histological sections of the LV from the apex (top left) to the base (bottom right) of PCL (H) and Piezo (I) groups, at 30 dpmi. Scar tissue is visible in blue, contrasting with the red-stained myocardium. Scale bar: 2 mm. (J) Infarct size, determined by infarct area (left) and midline length (right) for the patch-implanted groups and a MI-only control. (K) LV free wall thickness for the same groups plus a Sham control group. Values are presented as mean ± SEM. Sham: n = 3; MI-only: 9; PCL: n = 8; Piezo: n = 7. *p < 0.05, **p < 0.01, ****p < 0.0001. Note: in all cases, the fibers are placed between the PCL nanofilm and the cardiac tissue however, to simplify the visual representation of the fiber orientation, some schemes (A) show the fibers as if they are on top of the nanofilm. Statistical analysis: ordinary one-way ANOVA with Tukey's multiple comparisons test (J and K). (For interpretation of the references to colour in this figure legend, the reader is referred to the Web version of this article.)

electrical optical mapping or multi-electrode array (MEA) analyses.

3.4. Implantation of piezo patches in infarcted mice

To assess the effect of the Piezo patches *in vivo*, they were implanted in mice after MI induction. It should be mentioned that, even though there are technical and practical differences on using rat or mouse models, they are quite similar regarding cardiac physiology and pathology (e.g. in terms of contractility and electrophysiology) [54]. As performed in the *ex vivo* studies, Piezo and PCL patches were directly glued to the epicardium by means of fibrin glue and a biopsy punch (Figs. S6A–D) (Movie S3). This method allowed the adjustment of fiber

orientation before implantation while the patch became stretched and adhered to the epicardium, being deformed synchronously with the heart cycle (Fig. S6D) (Movie S3). Of note, according to previous studies it is unlikely that fibrin glue impairs electrical conductivity [55]. Patches remained adhered to the epicardium at least 7 days after surgery, with the PVDF-TrFE fibers being visible and in close contact with the myocardium (Figs. S6E–J). Furthermore, the orientation of the fibers was consistent with the known oblique alignment of sub-epicardial fibers (Fig. S7) which was intended due to the anisotropic nature of electrical charge generation in piezoelectric materials.

3.5. *Effect of piezo patches on mice cardiac tissue function and remodeling after MI*

To determine the electrophysiological and contractility impact of Piezo patches *in vivo*, they were implanted in mice immediately after MI induction (Fig. 4A and 5A) (Movie S4), and compared to control PCL patches, which shared the same PCL nanofilm support and presented similar fibril conformation, whilst lacking the piezoelectric effect. It should be noted that, although non-transplanted MI mice were also included as a reference control, these animals were submitted to a shorter surgical procedure, with less cardiac manipulation, and were not

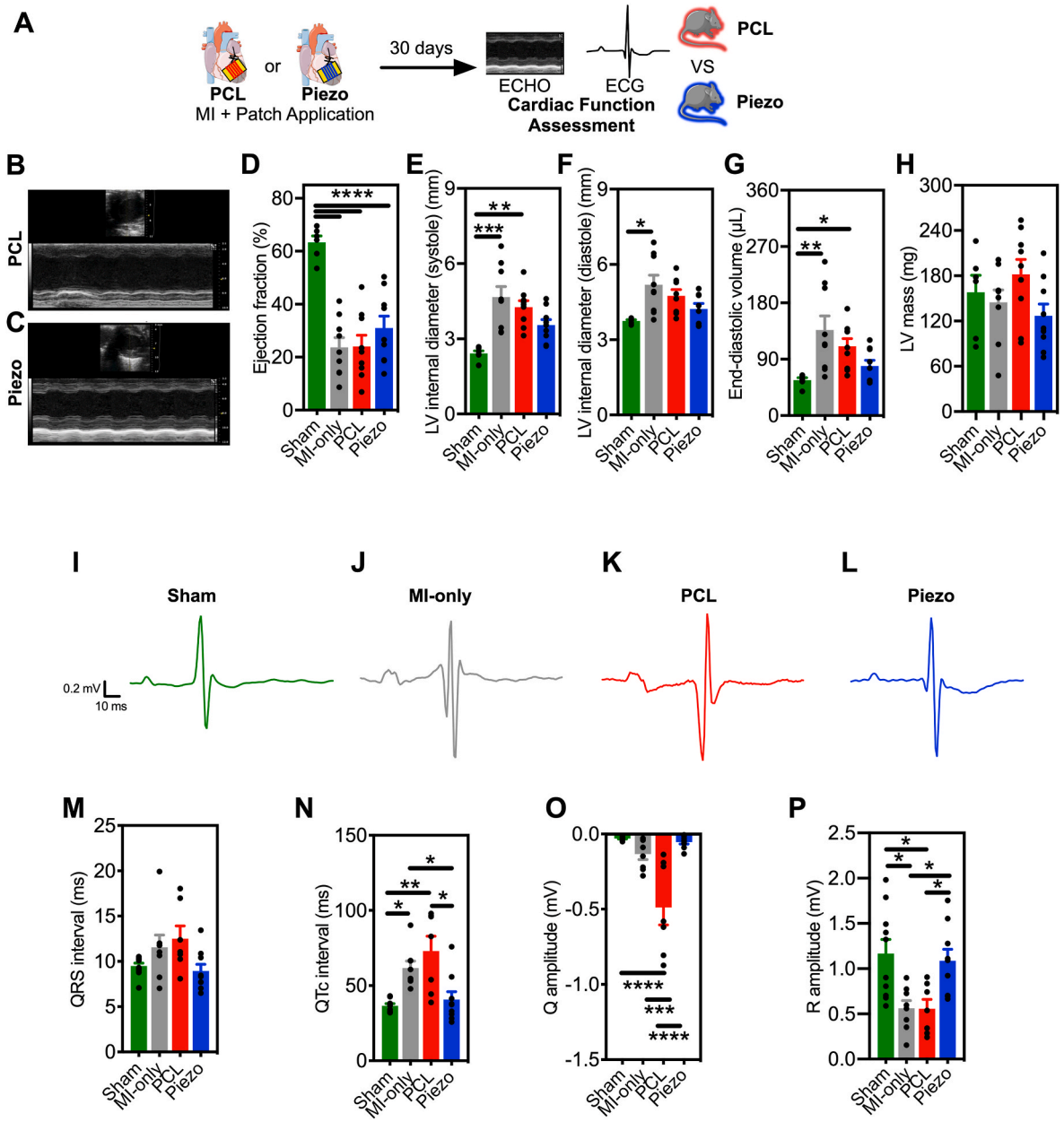

Fig. 5. *In vivo* evaluation of piezo patch on cardiac function. (A) Experimental procedure and timeline leading to cardiac function assessment. (B to H) Transthoracic echocardiography. Representative M (Motion)-mode images in SAX (Short-axis) view of both PCL (B) and Piezo (C) groups, at 30 dpmi. Echocardiographic parameters comparing the patch-implanted groups and Sham and MI-only controls: ejection fraction (D), LV internal diameter during systole (E), LV internal diameter during diastole (F), End-diastolic volume (G), and LV mass (H). (I to P) Surface electrocardiography (ECG). (I–L) Representative ECG signal traces of Sham (I), MI-only (J), PCL (K) and Piezo (L) groups. (M to P) ECG parameters comparing the experimental groups: QRS interval (M), QTc interval (N), Q amplitude (O), and R amplitude (P). All values are presented as mean ± SEM. Sham: n = 6; MI-only: n = 11; PCL: n = 9; Piezo: n = 9 * $p < 0.05$, **$p < 0.01$* $p < 0.05$, **$p < 0.01$, ***$p < 0.001$, ****$p < 0.0001$. No outliers were identified. Note: in all cases, the fibers are placed between the PCL nanofilm and the cardiac tissue however, to simplify the visual representation of the fiber orientation, some schemes (A) show the fibers as if they are on top of the nanofilm. Statistical analysis: ordinary one-way ANOVA with Tukey's multiple comparisons test (D, H, M, O, P); Krustal-Wallis test with Dunn's multiple comparisons test (E, F, G, N).

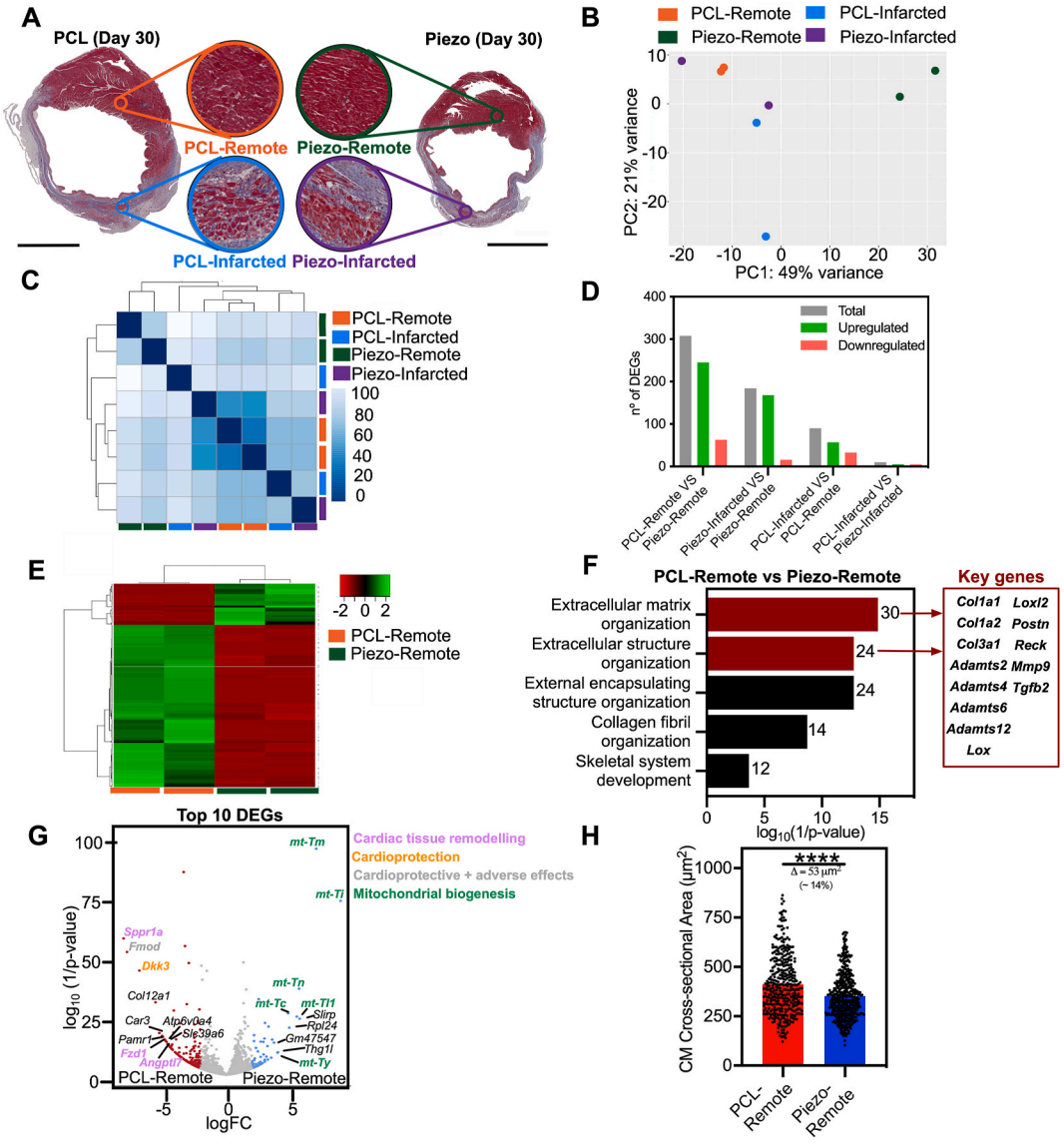

Fig. 6. Transcriptomic Profiling of Spatially-Defined Cardiac Tissue Regions by RNASeq. (A) Visual representation of the different tissue regions microdissected and processed for RNASeq. (B) Principal Component Analysis (PCA) plot. (C) Unsupervised clustering showing sample-to-sample distances heatmap representation of the comparison between all samples. Color code represents row Z-Score. (D) Number of Differentially Expressed Genes (DEGs) (total, downregulated and upregulated) (of the first condition relative to the second) revealed following relevant pairwise comparisons between RNASeq data of different conditions. (E) Heatmap representation or the PCL-Remote vs Piezo-Remote comparison. Color code represents row Z-Score. (F) Gene Ontology (GO) analysis (Biological Process) for genes upregulated in PCL-Remote relative to Piezo-Remote. The number of genes associated with each gene set is displayed. Respective $\log_{10}$(1/p-value) values derive from adjusted p-values. (G) Volcano Plot exhibiting upregulated (red) and downregulated genes (blue) in PCL-Remote relative to Piezo-Remote ($|\log_2 FC|>2$; p-value<0.05). Top 10 differentially expressed genes (regarding fold-change) have their name displayed. RNASeq data: n = 2 samples per animal, n = 1 animal per experimental group. (H) Quantification of cardiomyocyte cross-sectional area on the PCL-Remote and Piezo-Remote histological regions. Values are presented as mean ± SEM. PCL: n = 380; Piezo: n = 472 cardiomyocytes from a total of n = 3 animals per experimental group, ****p < 0.0001. In H, five outliers were excluded from PCL-Remote and twenty-five outliers were removed from Piezo-Remote. Statistical analysis: Mann Whitney test (H). (For interpretation of the references to colour in this figure legend, the reader is referred to the Web version of this article.)

subjected to any epicardial implantation. Circular patches had a diameter of around 4 mm which allowed coverage of ischemic and non-ischemic regions of the heart. At the end-point we show that the infarcted tissue is largely covered by the PCL and Piezo (Fig. S8A) and that approximately 16.8 % and 18.5 % of the PCL and Piezo patches, respectively, was able to cover a non-ischemic region (Fig. S8B). At day 30 post-implantation, the animals were evaluated by both ECHO and surface ECG and sacrificed for evaluating the biomaterial-tissue interface and LV remodeling using histology (Fig. 4). In both groups, patches remained adhered to the epicardial surface of the heart until the end of the experiment.

To evaluate cardiac remodeling, morphometric analyses of representative LV histological sections were performed (Fig. 4B–K). Both patch-implanted groups show a tendency to have smaller infarcts and increased LV free wall thickness than the non-implanted MI control group (MI-only) (Fig. 4J and K). The level of fibrosis/infarct (as assessed by infarct area and midline length) and LV free wall thickness showed no statistical differences between PCL and Piezo groups (Fig. 4J and K).

The identity of the cells in the proximity of the PCL and Piezo patches was assessed by immunofluorescence, showing cellular diversity, including abundant immune cells ($CD45^+$), fibroblasts ($vimentin^+$) and endothelial cells ($CD31^+$) (Figs. S9A and B). Of note, no notable differences were found between the PCL and Piezo groups (Figs. S9A and B).

To evaluate heart function, ECHO analyses were performed

(Fig. 5A–H). ECHO parameters have been widely in the literature as an assessment of the therapeutic efficiency of a plethora of therapeutic strategies applied to rodent models of myocardial infarction [56,57]. In terms of systolic function, a tendency for increased ejection fraction (EF) was observed in the Piezo group when compared to the PCL and the non-implanted MI control groups (Fig. 5D), suggesting improved myocardial performance. Moreover, both patch-implanted groups had more favorable (although without statistical significance) LV internal diameters (Fig. 5E and F) and end-diastolic volume (EDV) (Fig. 5G) than the MI-only group. Notably, when compared with the PCL group, the Piezo-treated animals exhibited less evident adverse cardiac remodeling as strong tendency for a decrease in LV internal diameter in systole (Fig. 5E), LV internal diameter in diastole (Fig. 5F), EDV (Fig. 5G), and LV mass (Fig. 5H); being indicative that the Piezo have less LV cavity dilatation, an hallmark of adverse cardiac remodeling process. These findings are suggest that the Piezo group has a reduced compensatory hypertrophy an adaptive mechanism to compensate for increased wall tension.

To further assess whether Piezo patches promoted cardiac electrical improvement after MI, surface ECGs were captured (Fig. 5A–I-P and S10). The differences between Piezo and PCL-implanted groups are significant. Piezo-implanted group showed less adverse electrical remodeling (Fig. 5I–P) with a tendency for a less prolonged QRS interval (Fig. 5M), and a significantly less prolonged QTc interval (Fig. 5N) as compared to animals treated with the PCL patch. Notably, Piezo group showed a practically absent Q wave and increased R amplitude (Fig. 5O and P). PCL-implanted group showed an electrical impairment compared to a non-transplanted MI animal group considering some ECG parameters (Fig. 5I–P and S10) likely due to differences in the surgical procedure (see above). Yet, Piezo-implanted group showed improved ECG parameters (e.g. QTc interval and R amplitude) when compared to the MI-only group and similar with the Sham control group (Fig. 5N–P), further highlighting the effect of the Piezo patch regardless of the surgical conditions. Of note, no differences were observed in terms of heart rate (Fig. S10A), PR interval (Fig. S10B), or P amplitude (Fig. S10C). Assessment of Connexin-43 protein expression patterns showed that although intercellular coupling was defective in peri-infarct myocardial regions near the patch when compared to remote myocardial regions, no apparent differences were detected between experimental groups (Fig. S11). Overall, these results show that the Piezo patches induced clinically relevant improvements on cardiac electrical integrity while compared to PCL patches.

Taken together, our *in vivo* results suggest that the Piezo group, when compared to PCL, exhibits: i) less adverse cardiac remodeling (decreased LV dilation and compensatory hypertrophy); and ii) more efficient ventricular repolarization which may decrease the risk of ventricular arrhythmias and, consequently, of the occurrence of arrhythmia-related sudden death [58,59]. Importantly, decreased cardiac remodeling and higher cardiac electrical integrity observed in animals treated with Piezo patches resulted in modest improvements in systolic function. One can speculate that a longer follow-up would be necessary to obtain a more pronounced effect of the observed remodeling and electrophysiological improvements on cardiac contractility. We hypothesize that the Piezo patches may improve cardiac action potential transmission between infarct border regions, bypassing the main infarcted regions, thus contributing to strengthen electrical stimulation of the non-ischemic myocardium that strongly contributes to LV contractility. Our results strongly support the safety of these electroactive patches as no adverse effects were observed at the tissue and functional levels following implantation. Similar results have been reported for conductive patches for which no difference was observed in cardiac function between controls and patch treatment [7]. Finally, this work reports, for the first time, the *in vivo* safety and cardiac electrical conduction improvements in the context of MI of an electroactive piezoelectric patch-based strategy.

3.6. Effect of piezo patches on the molecular program of mice ischemic and remote myocardium

To explore the impact of Piezo patch implantation in the myocardial molecular program after MI, we performed RNASeq analysis. For this purpose, two different areas (*ca.* 5×10^5 μm2; all sort of cardiac cells) of the LV, one in the infarcted region near the patch (infarcted) and the second on the remote myocardium (remote) were collected by laser capture microdissection (LCM) and the whole-transcriptome was compared by RNASeq (Fig. 6A). Information about RNA quality and integrity of the sequenced samples is presented in Fig. S12. Library construction and sequencing workflow are described in the *Material and Methods* (subsection 2.13.4. *Library construction and sequencing*) and as a scheme in Fig. S13. Principal component analysis (PCA) (Fig. 6B) and unsupervised clustering of the samples (Fig. 6C) show that Piezo-Remote samples were segregated from the remaining groups. Surprisingly, no discrimination was observed between ischemic versus remote regions, as could be initially argued. In terms of differentially expressed genes (DEG), PCL-Remote vs Piezo-Remote was the pairwise comparison that retrieved the most differences (308 DEG), followed by Piezo-Infarcted vs Piezo-Remote (184 DEG), PCL-Infarcted vs. PCL-Remote (90 DEG) and finally PCL-Infarcted vs. Piezo-Infarcted (10 DEG) (Fig. 6D). Hence the main differences between the two patches were observed in the remote myocardium rather than in ischemic regions near implantation. These results are in consonance with differences observed for LV mass (Fig. 5H) and in electrophysiological parameters (Fig. 5L–Q) that can only be explained by an effect of the patch in remote myocardial regions. To disclose the underlying mechanisms we focused our analysis on the comparison between PCL- and Piezo-Remote regions (Fig. 6E–H). Gene Ontology (GO) enrichment analysis highlighted significantly altered pathways/biological processes (Fig. 6F). Interestingly, compared to Piezo-Remote, PCL-Remote showed significantly upregulated gene sets associated with Extracellular matrix organization; Extracellular structure organization; and Collagen fibril organization. This observation highlights that the PCL group was more affected by cardiac remodeling in the remote region than its Piezo counterpart. Importantly, this panel comprises gene-sets for structural components of the extracellular matrix (ECM) including: Extracellular matrix organization (GO:0030198) (*Adamts2, Adamts6, Adamts12, Bgn, Cd44, Col1a1, Col1a2, Col3a1, Col4a3, Col5a1, Col5a2, Col8a1, Col12a1, Col27a1, Ctsk, Fbn1, Fn1, Lox, Loxl2, Mmp9, P4ha3, Postn, Reck, Sh3pxd2b, Smoc1, Tgfb2, Thsd4, Vcam1, Vcan*); Extracellular structure organization (GO:0043062) (*Adamts2, Adamts4, Adamts6, Adamts12, Bgn, Cd44, Col1a1, Col1a2, Col3a1, Col4a3, Col5a1, Col5a2, Col8a1, Col27a1, Fbn1, Fn1, Lox, Mmp9, Postn, Reck, Smoc1, Thsd4, Vcam1, Vcan*); and Collagen fibril organization (GO:0030199) (*Adamts2, Col1a1, Col1a2, Col3a1, Col4a3, Col5a1, Col5a2, Col8a1, Col12a1, Col27a1, Lox, Loxl2, P4ha3, Tgfb2*). This observation highlights that the PCL group was more affected by cardiac remodeling in the remote region than its Piezo counterpart. The upregulation of these transcripts comprise not only structural components of the extracellular matrix (ECM) (e.g *Col1a1, Col1a2, Col3a1)* corresponding to collagens type I and III, the most abundant in the heart and MI [60]) but also for enzymes, matricellular components, transmembrane proteins and growth factors that regulate ECM remodeling. Of note, these genes have been described to play key roles in the context of MI, such as increased cell death, fibrosis and/or cardiac hypertrophy (*Adamts2* [61], *Adamts4* [61], *Adamts6*, *Adamts12* [61], *Lox*, *Loxl2*, *Postn* [62]), cardioprotection (*Reck* [63], *Cd44* [64]), and a combination of both effects, in a cell-type and/or context-dependent manner (*Mmp9* [65], *Vcam1* [66,67], *Tgfb2* [68,69]).

Analysis of the DEG with higher fold change between the two groups (Fig. 6G) highlighted genes associated with mitochondria and/or mitochondrial biogenesis upregulated in Piezo-Remote [70] (*mt-Ti*, *mt-Tm*, *mt-Tn*, *mt-Tl1*, *mt-Tc* and *mt-Ty*), suggesting that mitochondrial function and biogenesis might be affected in their PCL-Remote counterpart and/or, potentially, its metabolic activity. Importantly, the top 10

upregulated genes in PCL-Remote were related to maladaptive cardiac tissue remodeling (*Sprr1a* [71], *Angptl7* [72], *Fzd1* [73]), to cardioprotection (*Dkk3* [74]) and with both cardioprotective and adverse effects (*Fmod* [75]). Importantly, *Sprr1a*, the most overexpressed gene in PCL-Remote, that encodes for the small proline-rich protein 1a (SPRR1A), or cornifin-A, has been reported to be upregulated post-MI [71], not only being overexpressed in CMs and cardiac fibroblasts isolated from mice subjected to MI, but also in patients with heart failure with reduced ejection fraction (HFrEF). It was reported that *Sprr1a* knockdown in MI mice had a cardioprotective effect. This gene is also one of the targets inhibited by the microRNA-150 (miR-150), known to be cardioprotective, being its deletion associated with maladaptive cardiac remodeling, that included increased cell death and cardiac hypertrophy. Of note, both *Dkk3* and *Fzd1* genes are associated with the WNT signaling pathway. The activation of this signaling pathway has been widely associated with maladaptive cardiac remodeling post-MI, including exacerbated inflammatory response, and increased fibrosis and hypertrophy, and impaired cardiac function [76]. Frizzled class receptor 1 (FZD1), a receptor that mediates the activation of the WNT pathway promoted cardiac hypertrophy and the decline of cardiac function in a mouse model of MI [73]. In contrast, dickkopf-3 (DKK3), an antagonist of the WNT signaling, was shown to be cardioprotective in a MI mouse model [74]. This reveals that PCL-Remote, in comparison to Piezo-Remote, presents alterations on the balance of the WNT signaling pathway, possibly because of the undergoing cardiac remodeling process. To further understand the biological processes that could be connected with the gene upregulation seen in both Piezo-Remote and PCL-Remote, we ascertained the protein-protein interactions that could be expected from the proteins encoded by said differently expressed genes. For that purpose, we resorted to STRING (https://string-db.org), a database composed of known and predicted protein-protein interactions. This analysis unveiled a major cluster in the PCL-Remote (Fig. S14). This agglomerate shows interconnected interactions between several genes/proteins associated with cardiac ECM remodeling (e.g. collagens, proteoglycans, pro-fibrotic factors, elements of the WNT signaling pathway).

Apart from genes described above, other genes/proteins associated with cardiac remodeling were further highlighted such as *Serpine2* [77], *Nppa* [78] and *Nrg* [79], further strengthening that the cardiac tissue region remote from the injury/patch application site in the PCL group (PCL-Remote), in comparison with its Piezo counterpart, was undergoing several changes associated with cardiac tissue remodeling. For instance, the *Nppa* gene encodes for the atrial natriuretic factor (ANF), a natriuretic peptide mainly secreted by the atrial tissue when stretched, which is widely used as surrogate marker of cardiac overload and adverse outcome in heart failure patients [78,80,81]. Moreover, neuroregulin-1 (NRG1), a paracrine growth factor secreted by endothelial cells upon cardiac injury, has been linked to promote fibrosis and hypertrophy during early cardiac remodeling in a pressure overload mouse model [82], and to induce hypertrophy and cardiac function impairment in rats subjected to MI [79]. However, its effects are still not fully understood, as it is also been shown to be cardioprotective in the context of heart failure in a large animal model [83] and has even been considered as a potential future therapy [84], and tested in clinical trials (ClinicalTrials.gov, NCT04391491, NCT01439789, NCT01214096).

Taken together, the transcriptomic analysis revealed that the cardiac tissue region remote from the injury/patch application site in the PCL group (PCL-Remote), in comparison with its Piezo counterpart (Piezo-Remote), was undergoing several changes associated with cardiac tissue remodeling, as several genes often upregulated in the context of MI and other heart failure models were also overexpressed in PCL-Remote (e.g. collagens, proteoglycans, ECM remodeling enzymes, WNT signaling pathway elements, growth factors). However, it is not possible to conclude whether this balance of the several overexpressed factors represents, mostly, an undergoing maladaptive remodeling process (i.e. more hypertrophic and fibrotic) or a cardioprotective one, as molecular players associated with both scenarios were upregulated, along with others with dual, context-dependent or even controversial/doubtful roles.

Considering that the functional results showed an increase in the LV mass in the PCL group, we analyzed whether the histology sections revealed cardiomyocyte hypertrophy on the myocardial region far from the Patch, on the PCL group. In fact, the cardiomyocyte cross-sectional area of PCL-Remote was significantly increased (by ~12 %) when compared with Piezo-remote section (Fig. 6H), thus corroborating the hypothesis that Piezo patch promotes healthier remodeling, leading to less strain exerted on healthy region of the LV.

To date, the cellular and molecular impact of piezoelectric patches and of conducting materials [6,7] in the heart is largely unknown. Even though this transcriptional analysis is exploratory in nature (one biological replicate), it provides, for the first time, molecular information about the effect of piezoelectric patches at the lesion site as well as far from the lesion, where it activated mitochondrial biosynthesis whilst downregulating ECM-associated transcripts. This is in agreement with the fact that the activation of mitochondrial biosynthesis counteracts the glycolysis typically observed upon cardiac hypertrophy and heart failure [85–87]. Importantly, these alterations translated to improved cardiac electric integrity and attenuated remodeling when compared to non-electroactive patches (PCL control).

3.7. *In vivo implantation and electrical safety assessment of Piezo patches in non-disease or MI pig hearts*

To assess the applicability and electrical safety of the Piezo patches in the heart of a large animal model, we proceeded to an *in vivo* implantation of PCL and Piezo patches in non-disease or infarcted pig hearts (Fig. 7A and B), followed by the evaluation of the patch effects on cardiac electrical safety immediately after implantation (Fig. 7C–E). Importantly, the patches were successfully applied in the epicardium of the pig hearts through an open-chest procedure (Fig. 7B; Movie S5). Moreover, to evaluate the safety of the Piezo patches in a non-disease or MI porcine heart model in terms of electrical integrity and arrhythmogenicity, epicardial ECG signals were obtained from the base and apex of the pig hearts before (baseline) or immediately after applying either one of the PCL or Piezo patches (Fig. 7C–E). In that way, the safety profile of the patches was evaluated in terms of variations in the cardiac action potential propagation time between the base and apex of the heart (Δt) having the QRS peak as a reference (Fig. 7D and E). Importantly, the application of either PCL or Piezo patches did not cause statistically significant variations in base-to-apex action potential propagation time (*i.e.* Δt), although the PCL control patches caused a slight delay in healthy hearts when compared with the Piezo patches (Fig. 7D). Of note, no arrhythmias were detected during the ECG acquisition and procedures (data not shown).

Considering the PCL and Piezo patches have small dimensions when compared with the porcine myocardium, we performed a proof-of-concept experiment with larger patches (2 × 2.5 cm vs. 7.5 × 6.0 cm) to assess the feasibility of implanting patches with clinically relevant dimensions (Fig. S15). To upscale the dimensions of the patches, so that its area would be more compatible and relevant when considering the pig myocardial tissue mass, we first increased the size of both the silicon wafer substrates and of the rotating collector from the electrospinning system (Figs. S15A and B), resulting in an increase of the total initial area of the patches (i.e. before implantation) by 9-fold, and the initial area of the patch effectively coated with fibers by 12-fold (Fig. S15A). Finally, by means of an open-chest procedure applied to a pig model we show that the patches were successfully applied to a beating non-disease pig heart (Fig. S15C; Movie S6). Notably, although other cardiac patches have been tested in swine heart models [88–91], our Piezo patches are larger than previously reported patches (e.g. 5.0 × 5.0 cm [88]; 5.0 × 2.0 cm [89]; Ø = 3.5 cm [90]), therefore exhibiting a more clinically relevant size, and are the first piezoelectric cardiac patches applied in

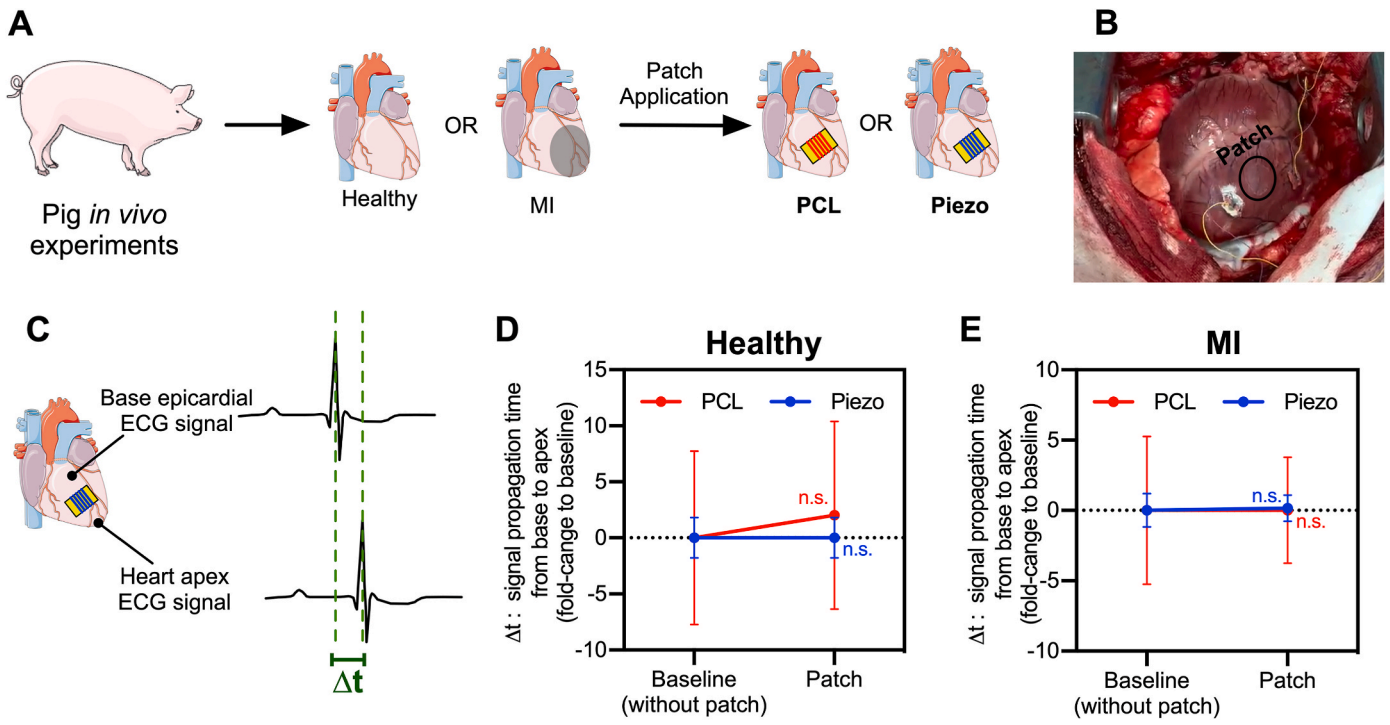

Fig. 7. – *In vivo* ECG-based electrical integrity proof-of-concept safety assessment of the PCL and Piezo patches in a porcine large animal model. (A–D) *In vivo* patch application of patches in healthy or infarcted pig hearts (A and B) and the assessment of their effect on cardiac electrical propagation properties by means of epicardial ECG signals measured in the heart's base and apex, immediately after implantation (C). (D and E) Before-after graphs representing the effect of the patches in the cardiac electrical propagation, in either healthy (D) or infarcted (E) pig hearts, by determining the change in the time difference between the peaks from the epicardial ECG signals from the heart's base and apex (Δt), after adding either PCL or Piezo patches. PCL: n = 4; Piezo: n = 5 measurements. Values are presented as mean ± SEM. Statistical analysis: 2way ANOVA (D and E).

porcine hearts, to our knowledge). Of note, no arrhythmias were detected during the ECG acquisition and procedures (data not shown).

Considering the similarities between pig and human hearts in terms of size and electrophysiology [92], the present results are initial evidence of the potential of using Piezo patches in a clinical setting, in terms of implantability and electrical safety since we did not detect arrhythmogenic effects. Nevertheless, one should be cautious and take into account the limitations of the porcine heart experiments, as it comprises a proof-of-concept safety assessment with a limited number of animals and performed in an acute setting.

4. Conclusions

The current study shows that Piezo cardiac patches may (i) be directly applied to viable cardiac tissue (implantability) without compromising its function (safety) and (ii) benefit infarcted hearts at functional, cellular and molecular levels. At functional level, Piezo patch enhanced electrical integrity. At cellular/tissue levels, Piezo patch improved cardiac tissue remodeling as shown by the decreased LV internal diameter in systole and LV mass and decreased cross-sectional area of the cardiomyocytes. At molecular level, animals implanted with Piezo patches showed an upregulation of genes associated with mitochondrial biosynthesis and downregulation of genes linked with ECM remodeling, far from the lesion site, and these alterations indicate the emergence of tissue repair processes.

Piezo patches can be directly applied to viable cardiac tissue without compromising its function. Previous studies have demonstrated that cardiac patches with excessive stiffness can, in certain instances, restrict heart movement, thereby impairing its function [93]. Future research should delve deeper into the potential mechanical constriction associated with our patches. However, it is crucial to note that, for some parameters, the Piezo patches exhibited improvements compared to the patch-free myocardial infarction group. Moreover, *ex vivo* (rat heart model and rat cardiac slices) and *in vivo* (mouse and pig MI models) experiments showed that this biomaterial does not preclude tissue function in a short timeframe. Our results further show the successful application of Piezo patches (with variable dimension) in a non-disease and/or infarcted porcine hearts without compromising its electrophysiology. Nevertheless, other ECG monitoring methods, such *in vivo* implantable telemetry devices, could be more useful in ascertaining whether any abnormal changes in beating would appear during the 30 days of the *in vivo* experiment. However, due to technical limitations, such as the reduced size of the mouse hearts and ethical concerns on performing additional surgical implantation procedures after inducing MI and placing the patch, telemetry devices were not implanted. Another important area for future investigation is the *in vivo* degradation of the piezo patch. Our findings suggest that the piezoelectric fibers remained intact after 30 days of *in vivo* experimentation, although we were unable to monitor the degradation of the nanofilm due to its nanometer thickness. Yet, in a separate *in vitro* study, using identical PCL nanofilms, demonstrated stability for at least 12 days while exposed to cell culture conditions, including contact with cell culture medium and cardiac cells [24].

Epicardial implantation of the piezoelectric patch in an *in vivo* model of MI showed an attenuation of cardiac remodeling and a strong improvement of cardiac electrical integrity. When compared to control patches, Piezo patches alter the molecular program of cardiac cells at non-ischemic regions of the heart, promoting a more favorable cardiac repair and remodeling. Our results emphasize that future studies should investigate not only the lesion area (infarcted region) but also cardiac tissue outside the lesion area (non-infarcted region) when investigating cardiac patch regenerative potential.

Our study shows for the first time the possibility to harness the contractile motion of the myocardium to electrically stimulate the same

tissue for improving its electrophysiological function. So far, most *in vivo* uses for piezoelectric materials in the heart were for mechanical energy harvesting [25,26] and, only recently, their therapeutic potential was assessed for the first time in an *in vivo* model of MI by Han et al. [20]. In the latter study, the authors implanted cell-laden piezoelectrical patches in the hearts of a rat model MI and showed that they improved systolic function and reduced infarction size, however did they not assess the effect on electrophysiological function (e.g. ECG) nor alterations in the molecular program [20]. In contrast, in our present work, we filled that significant knowledge gap by (i) showing clear improvements in the electrophysiological function in a mouse model of MI and by (ii) unveiling alterations in the molecular program that were associated with the functional improvements. Importantly, it is noteworthy to mention that while the Han et al. utilized cell-laden cardiac construct, here we show for the first time that the piezoelectrical material alone promotes functional improvement and exerts positive therapeutical effects.

Considering we observed improvements in several ECG parameters and observed apparently beneficial changes in gene expression in the heart region farthest from the patch (when compared to the PCL controls), we hypothesize that the electrical field generated by the Piezo patches was not sufficiently strong to cause a negative disruption of the normal heart electrical activity, but it was potentially effective enough to stimulate the survival and activity of the cardiomyocytes which were subjected to this patch-derived electrical stimulation. Further studies will be required to evaluate how much electrical signal is transmitted from the piezo patch to the epicardium and then to the myocardium. Additionally, further studies are needed to assess the long-term effects of the patch on heart function. Our findings indicated that the short-term functional effects, such as ejection fraction, were limited in animals treated with the piezo patch compared to those receiving the control patch.

Grounded on previous evidence showing that these biomaterials are compatible with rodent and human cardiomyocytes [24] and the results by Han et al. *al.* [20], future tissue engineering-based approaches involving the implantation of this electroactive piezoelectric patch pre-seeded with mature and functionally active cardiomyocytes, could have synergistic effects on the overall electromechanical activity of an infarcted heart. In addition, in the future, bioactive factors can be loaded in the patches among the fibers, where the underlying PCL nanofilms would be beneficial in preventing these factors from being diffused out of the epicardium, thus rendering the delivery system more efficient.

CRediT authorship contribution statement

Luís M. Monteiro: Writing – original draft, Visualization, Investigation, Formal analysis, Conceptualization. **Pedro J. Gouveia:** Writing – review & editing, Methodology, Conceptualization. **Francisco Vasques-Nóvoa:** Writing – review & editing, Resources, Methodology, Investigation, Formal analysis, Conceptualization. **Susana Rosa:** Investigation. **Ifigeneia Bardi:** Methodology, Investigation, Conceptualization. **Rita N. Gomes:** Writing – review & editing, Visualization, Formal analysis. **Simão Correia-Santos:** Investigation. **Leonardo Ricotti:** Writing – review & editing, Supervision, Resources, Methodology, Conceptualization. **Lorenzo Vannozzi:** Writing – review & editing, Methodology, Investigation, Formal analysis, Conceptualization. **Daniele Guarnera:** Methodology, Investigation, Formal analysis. **Liliana Costa:** Investigation. **André M. Leite-Moreira:** Writing – review & editing, Resources, Methodology, Investigation, Conceptualization. **Pedro Mendes-Ferreira:** Writing – review & editing, Resources, Methodology, Investigation, Conceptualization. **Adelino F. Leite-Moreira:** Writing – review & editing, Supervision, Resources. **Filippo Perbellini:** Writing – review & editing, Supervision, Resources, Methodology, Conceptualization. **Cesare M. Terracciano:** Writing – review & editing, Supervision, Resources, Conceptualization. **Perpétua Pinto-do-Ó:** Writing – review & editing, Resources, Conceptualization. **Lino Ferreira:** Writing – review & editing, Visualization, Supervision, Resources, Project administration, Funding acquisition, Conceptualization. **Diana S. Nascimento:** Writing – review & editing, Supervision, Resources, Project administration, Methodology, Funding acquisition, Conceptualization.

Declaration of competing interest

The authors declare that they have no known competing financial interests or personal relationships that could have appeared to influence the work reported in this paper.

Acknowledgment

This work was funded by FEDER through the Program COMPETE and by Portuguese fund through FCT in context of the projects [PTDC/BTM-SAL/29229/2017], [POCI-01-0145-FEDER-016385] and[POCI-01-0145-FEDER-030985]. This work was also partly funded by the European Union (REBORN [G.A. 101091852], RESETageing [G.A: 952266] and ERAatUC [G.A. 669088]. Views and opinions expressed are however those of the author(s) only and do not necessarily reflect those of the European Union or the European Health and Digital Executive Agency [HADEA]. Neither the European Union nor the granting authority can be held responsible for them. The authors would also like to thank FCT for individual funding: LMM [SFRH/BD/129991/2017 and COVID/BD/151893/2021], SR [DOI 10.54499/DL57/2016/CP1448/CT0018], RG [SFRH/BD/144490/2019] and DSN [CEECINST/00091/2018]. There are no conflicts to declare.

Appendix A. Supplementary data

Supplementary data to this article can be found online at https://doi.org/10.1016/j.mtbio.2025.101742.

Data availability

Data will be made available on request.

References

[1] M.A. Khan, M.J. Hashim, H. Mustafa, M.Y. Baniyas, S. Al Suwaidi, R. AlKatheeri, F. M.K. Alblooshi, M. Almatrooshi, M.E.H. Alzaabi, R.S. Al Darmaki, S. Lootah, Global epidemiology of ischemic heart disease: results from the global burden of disease study, Cureus 12 (7) (2020) e9349.

[2] P. Menasche, Cell therapy trials for heart regeneration - lessons learned and future directions, Nat. Rev. Cardiol. 15 (11) (2018) 659–671.

[3] R.C. de Abreu, H. Fernandes, P.A. da Costa Martins, S. Sahoo, C. Emanueli, L. Ferreira, Native and bioengineered extracellular vesicles for cardiovascular therapeutics, Nat. Rev. Cardiol. 17 (11) (2020) 685–697.

[4] M.J. Hernandez, K.L. Christman, Designing acellular injectable biomaterial therapeutics for treating myocardial infarction and peripheral artery disease, JACC Basic Transl Sci 2 (2) (2017) 212–226.

[5] M. Montgomery, S. Ahadian, L. Davenport Huyer, M. Lo Rito, R.A. Civitarese, R. D. Vanderlaan, J. Wu, L.A. Reis, A. Momen, S. Akbari, A. Pahnke, R.K. Li, C. A. Caldarone, M. Radisic, Flexible shape-memory scaffold for minimally invasive delivery of functional tissues, Nat. Mater. 16 (10) (2017) 1038–1046.

[6] D. Mawad, C. Mansfield, A. Lauto, F. Perbellini, G.W. Nelson, J. Tonkin, S.O. Bello, D.J. Carrad, A.P. Micolich, M.M. Mahat, J. Furman, D. Payne, A.R. Lyon, J. J. Gooding, S.E. Harding, C.M. Terracciano, M.M. Stevens, A conducting polymer with enhanced electronic stability applied in cardiac models, Sci. Adv. 2 (11) (2016) e1601007.

[7] M. Kapnisi, C. Mansfield, C. Marijon, A.G. Guex, F. Perbellini, I. Bardi, E. J. Humphrey, J.L. Puetzer, D. Mawad, D.C. Koutsogeorgis, D.J. Stuckey, C. M. Terracciano, S.E. Harding, M.M. Stevens, Auxetic cardiac patches with tunable mechanical and conductive properties toward treating myocardial infarction, Adv. Funct. Mater. 28 (21) (2018) 1800618.

[8] L.M. Monteiro, F. Vasques-Nóvoa, L. Ferreira, P. Pinto-do-Ó, D.S. Nascimento, Restoring heart function and electrical integrity: closing the circuit, NPJ Regen. Med. 2 (1) (2017) 9.

[9] K. Hosoyama, M. Ahumada, C.D. McTiernan, D.R. Davis, F. Variola, M. Ruel, W. Liang, E.J. Suuronen, E.I. Alarcon, Nanoengineered electroconductive collagen-based cardiac patch for infarcted myocardium repair, ACS Appl. Mater. Interfaces 10 (51) (2018) 44668–44677.

[10] Q. Yin, P. Zhu, W. Liu, Z. Gao, L. Zhao, C. Wang, S. Li, M. Zhu, Q. Zhang, X. Zhang, C. Wang, J. Zhou, A conductive bioengineered cardiac patch for myocardial infarction treatment by improving tissue electrical integrity, Adv. Healthcare Mater. 12 (1) (2023) e2201856.
[11] Y. Zhao, P. Wang, Z. Chen, M. Li, D. Zhang, L. Yang, H. Li, Research progress of electrical stimulation in ischemic heart disease, Front. Cardiovasc. Med. 8 (2021) 761877.
[12] R.T. Borne, D. Katz, J. Betz, P.N. Peterson, F.A. Masoudi, Implantable cardioverter-defibrillators for secondary prevention of sudden cardiac death: a review, J. Am. Heart Assoc. 6 (3) (2017).
[13] T.J. Bunch, Who will benefit from an implantable cardioverter defibrillator? Circ Cardiovasc Qual Outcomes 12 (8) (2019) e005995.
[14] M.T. Chorsi, E.J. Curry, H.T. Chorsi, R. Das, J. Baroody, P.K. Purohit, H. Ilies, T. D. Nguyen, Piezoelectric biomaterials for sensors and actuators, Adv. Mater. 31 (1) (2019) e1802084.
[15] A. Cafarelli, A. Marino, L. Vannozzi, J. Puigmarti-Luis, S. Pane, G. Ciofani, L. Ricotti, Piezoelectric nanomaterials activated by ultrasound: the pathway from discovery to future clinical adoption, ACS Nano 15 (7) (2021) 11066–11086.
[16] A. Zaszczynska, A. Gradys, P. Sajkiewicz, Progress in the applications of smart piezoelectric materials for medical devices, Polymers 12 (11) (2020).
[17] M.H. Shamos, L.S. Lavine, Piezoelectricity as a fundamental property of biological tissues, Nature 213 (5073) (1967) 267–269.
[18] M. Minary-Jolandan, M.F. Yu, Nanoscale characterization of isolated individual type I collagen fibrils: polarization and piezoelectricity, Nanotechnology 20 (8) (2009) 085706.
[19] W.S. Williams, L. Breger, Piezoelectricity in tendon and bone, J. Biomech. 8 (6) (1975) 407–413.
[20] K. Han, M. Mao, L. Fu, Y. Zhang, Y. Kang, D. Li, J. He, Multimaterial printing of serpentine microarchitectures with synergistic mechanical/piezoelectric stimulation for enhanced cardiac-specific functional regeneration, Small (2024) e2401561.
[21] A.H. Rajabi, M. Jaffe, T.L. Arinzeh, Piezoelectric materials for tissue regeneration: a review, Acta Biomater. 24 (2015) 12–23.
[22] C. Ribeiro, V. Sencadas, D.M. Correia, S. Lanceros-Mendez, Piezoelectric polymers as biomaterials for tissue engineering applications, Colloids Surf. B Biointerfaces 136 (2015) 46–55.
[23] P. Hitscherich, S. Wu, R. Gordan, L.H. Xie, T. Arinzeh, E.J. Lee, The effect of PVDF-TrFE scaffolds on stem cell derived cardiovascular cells, Biotechnol. Bioeng. 113 (7) (2016) 1577–1585.
[24] P.J. Gouveia, S. Rosa, L. Ricotti, B. Abecasis, H.V. Almeida, L. Monteiro, J. Nunes, F.S. Carvalho, M. Serra, S. Luchkin, A.L. Kholkin, P.M. Alves, P.J. Oliveira, R. Carvalho, A. Menciassi, R.P. das Neves, L.S. Ferreira, Flexible nanofilms coated with aligned piezoelectric microfibers preserve the contractility of cardiomyocytes, Biomaterials 139 (2017) 213–228.
[25] C. Dagdeviren, B.D. Yang, Y. Su, P.L. Tran, P. Joe, E. Anderson, J. Xia, V. Doraiswamy, B. Dehdashti, X. Feng, B. Lu, R. Poston, Z. Khalpey, R. Ghaffari, Y. Huang, M.J. Slepian, J.A. Rogers, Conformal piezoelectric energy harvesting and storage from motions of the heart, lung, and diaphragm, Proc. Natl. Acad. Sci. U. S. A. 111 (5) (2014) 1927–1932.
[26] B. Lu, Y. Chen, D. Ou, H. Chen, L. Diao, W. Zhang, J. Zheng, W. Ma, L. Sun, X. Feng, Ultra-flexible piezoelectric devices integrated with heart to harvest the biomechanical energy, Sci. Rep. 5 (2015) 16065.
[27] Z. Liu, X. Wan, Z.L. Wang, L. Li, Electroactive biomaterials and systems for cell fate determination and tissue regeneration: design and applications, Adv. Mater. 33 (32) (2021) 2007429.
[28] M.A. Cavasin, Z. Tao, S. Menon, X.P. Yang, Gender differences in cardiac function during early remodeling after acute myocardial infarction in mice, Life Sci. 75 (18) (2004) 2181–2192.
[29] M.L. Lindsey, K.R. Brunt, J.A. Kirk, P. Kleinbongard, J.W. Calvert, L.E. de Castro Bras, K.Y. DeLeon-Pennell, D.P. Del Re, N.G. Frangogiannis, S. Frantz, R.J. Gumina, G.V. Halade, S.P. Jones, R.H. Ritchie, F.G. Spinale, E.B. Thorp, C.M. Ripplinger, Z. Kassiri, Guidelines for in vivo mouse models of myocardial infarction, Am. J. Physiol. Heart Circ. Physiol. 321 (6) (2021) H1056–H1073.
[30] A.B. Pullen, V. Kain, C.N. Serhan, G.V. Halade, Molecular and cellular differences in cardiac repair of male and female mice, J. Am. Heart Assoc. 9 (8) (2020) e015672.
[31] B. Bakrania, J.P. Granger, R. Harmancey, Methods for the determination of rates of glucose and fatty acid oxidation in the isolated working rat heart, J. Vis. Exp. 115 (2016).
[32] S.A. Watson, M. Scigliano, I. Bardi, R. Ascione, C.M. Terracciano, F. Perbellini, Preparation of viable adult ventricular myocardial slices from large and small mammals, Nat. Protoc. 12 (12) (2017) 2623–2639.
[33] S.A. Watson, J. Duff, I. Bardi, M. Zabielska, S.S. Atanur, R.J. Jabbour, A. Simon, A. Tomas, R.T. Smolenski, S.E. Harding, F. Perbellini, C.M. Terracciano, Biomimetic electromechanical stimulation to maintain adult myocardial slices in vitro, Nat. Commun. 10 (1) (2019) 2168.
[34] L.H. Michael, M.L. Entman, C.J. Hartley, K.A. Youker, J. Zhu, S.R. Hall, H. K. Hawkins, K. Berens, C.M. Ballantyne, Myocardial ischemia and reperfusion: a murine model, Am. J. Physiol. 269 (6 Pt 2) (1995) H2147–H2154.
[35] G. Buckberg, J.I. Hoffman, A. Mahajan, S. Saleh, C. Coghlan, Cardiac mechanics revisited: the relationship of cardiac architecture to ventricular function, Circulation 118 (24) (2008) 2571–2587.
[36] D.S. Nascimento, M. Valente, T. Esteves, F. de Pina Mde, J.G. Guedes, A. Freire, P. Quelhas, O.P. Pinto-do, MIQuant–semi-automation of infarct size assessment in models of cardiac ischemic injury, PLoS One 6 (9) (2011) e25045.
[37] J. Takagawa, Y. Zhang, M.L. Wong, R.E. Sievers, N.K. Kapasi, Y. Wang, Y. Yeghiazarians, R.J. Lee, W. Grossman, M.L. Springer, Myocardial infarct size measurement in the mouse chronic infarction model: comparison of area- and length-based approaches, J. Appl. Physiol. 102 (6) (2007) 2104–2111, 1985.
[38] R. Drmanac, A.B. Sparks, M.J. Callow, A.L. Halpern, N.L. Burns, B.G. Kermani, P. Carnevali, I. Nazarenko, G.B. Nilsen, G. Yeung, F. Dahl, A. Fernandez, B. Staker, K.P. Pant, J. Baccash, A.P. Borcherding, A. Brownley, R. Cedeno, L. Chen, D. Chernikoff, A. Cheung, R. Chirita, B. Curson, J.C. Ebert, C.R. Hacker, R. Hartlage, B. Hauser, S. Huang, Y. Jiang, V. Karpinchyk, M. Koenig, C. Kong, T. Landers, C. Le, J. Liu, C.E. McBride, M. Morenzoni, R.E. Morey, K. Mutch, H. Perazich, K. Perry, B.A. Peters, J. Peterson, C.L. Pethiyagoda, K. Pothuraju, C. Richter, A.M. Rosenbaum, S. Roy, J. Shafto, U. Sharanhovich, K.W. Shannon, C. G. Sheppy, M. Sun, J.V. Thakuria, A. Tran, D. Vu, A.W. Zaranek, X. Wu, S. Drmanac, A.R. Oliphant, W.C. Banyai, B. Martin, D.G. Ballinger, G.M. Church, C. A. Reid, Human genome sequencing using unchained base reads on self-assembling DNA nanoarrays, Science 327 (5961) (2010) 78–81.
[39] A.M. Bolger, M. Lohse, B. Usadel, Trimmomatic: a flexible trimmer for Illumina sequence data, Bioinformatics 30 (15) (2014) 2114–2120.
[40] D. Kim, J.M. Paggi, C. Park, C. Bennett, S.L. Salzberg, Graph-based genome alignment and genotyping with HISAT2 and HISAT-genotype, Nat. Biotechnol. 37 (8) (2019) 907–915.
[41] E. Afgan, D. Baker, B. Batut, M. van den Beek, D. Bouvier, M. Cech, J. Chilton, D. Clements, N. Coraor, B.A. Gruning, A. Guerler, J. Hillman-Jackson, S. Hiltemann, V. Jalili, H. Rasche, N. Soranzo, J. Goecks, J. Taylor, A. Nekrutenko, D. Blankenberg, The Galaxy platform for accessible, reproducible and collaborative biomedical analyses: 2018 update, Nucleic Acids Res. 46 (W1) (2018) W537–W544.
[42] M.V. Kuleshov, M.R. Jones, A.D. Rouillard, N.F. Fernandez, Q. Duan, Z. Wang, S. Koplev, S.L. Jenkins, K.M. Jagodnik, A. Lachmann, M.G. McDermott, C. D. Monteiro, G.W. Gundersen, A. Ma'ayan, Enrichr: a comprehensive gene set enrichment analysis web server 2016 update, Nucleic Acids Res. 44 (W1) (2016) W90–W97.
[43] E.Y. Chen, C.M. Tan, Y. Kou, Q. Duan, Z. Wang, G.V. Meirelles, N.R. Clark, A. Ma'ayan, Enrichr: interactive and collaborative HTML5 gene list enrichment analysis tool, BMC Bioinf. 14 (2013) 128.
[44] S. Babicki, D. Arndt, A. Marcu, Y. Liang, J.R. Grant, A. Maciejewski, D.S. Wishart, Heatmapper: web-enabled heat mapping for all, Nucleic Acids Res. 44 (W1) (2016) W147–W153.
[45] L. Raposo, R.J. Cerqueira, S. Leite, L. Moreira-Costa, T.L. Laundos, J.O. Miranda, P. Mendes-Ferreira, J.A. Coelho, R.N. Gomes, P. Pinto-do-Ó, D.S. Nascimento, A. P. Lourenço, N. Cardim, A. Leite-Moreira, Human-umbilical cord matrix mesenchymal cells improved left ventricular contractility independently of infarct size in swine myocardial infarction with reperfusion, Front. Cardiovasc. Med. 10 (2023).
[46] H.J. Motulsky, R.E. Brown, Detecting outliers when fitting data with nonlinear regression - a new method based on robust nonlinear regression and the false discovery rate, BMC Bioinf. 7 (2006) 123.
[47] W. Hiesinger, M.J. Brukman, R.C. McCormick, J.R. Fitzpatrick 3rd, J.R. Frederick, E.C. Yang, J.R. Muenzer, N.A. Marotta, M.F. Berry, P. Atluri, Y.J. Woo, Myocardial tissue elastic properties determined by atomic force microscopy after stromal cell-derived factor 1alpha angiogenic therapy for acute myocardial infarction in a murine model, J. Thorac. Cardiovasc. Surg. 143 (4) (2012) 962–966.
[48] P. Güthner, T. Ritter, K. Dransfeld, Temperature dependence of the piezoelectric constant of thin PVDF and P(VDF-TrFE) films, Ferroelectrics 127 (1) (1992) 7–11.
[49] C.C. Veerman, A.A. Wilde, E.M. Lodder, The cardiac sodium channel gene SCN5A and its gene product NaV1.5: role in physiology and pathophysiology, Gene 573 (2) (2015) 177–187.
[50] A.S. Amin, H.L. Tan, A.A. Wilde, Cardiac ion channels in health and disease, Heart Rhythm 7 (1) (2010) 117–126.
[51] Y. Xia, J.B. McMillin, A. Lewis, M. Moore, W.G. Zhu, R.S. Williams, R.E. Kellems, Electrical stimulation of neonatal cardiac myocytes activates the NFAT3 and GATA4 pathways and up-regulates the adenylosuccinate synthetase 1 gene, J. Biol. Chem. 275 (3) (2000) 1855–1863.
[52] M. Merentie, J.A. Lipponen, M. Hedman, A. Hedman, J. Hartikainen, J. Huusko, L. Lottonen-Raikaslehto, V. Parviainen, S. Laidinen, P.A. Karjalainen, S. Yla-Herttuala, Mouse ECG findings in aging, with conduction system affecting drugs and in cardiac pathologies: development and validation of ECG analysis algorithm in mice, Phys. Rep. 3 (12) (2015).
[53] J. Gehrmann, S. Frantz, C.T. Maguire, M. Vargas, A. Ducharme, H. Wakimoto, R. T. Lee, C.I. Berul, Electrophysiological characterization of murine myocardial ischemia and infarction, Basic Res. Cardiol. 96 (3) (2001) 237–250.
[54] A.G. Edwards, W.E. Louch, Species-dependent mechanisms of cardiac arrhythmia: a cellular focus, Clin. Med. Insights Cardiol. 11 (2017) 1179546816686061.
[55] M. Mehdikhani, S. Ghaziof, Electrically conductive poly-$${\upepsilon }$ $-caprolactone/polyethylene glycol/multi-wall carbon nanotube nanocomposite scaffolds coated with fibrin glue for myocardial tissue engineering, Appl. Phys. A 124 (1) (2018) 77.
[56] R.J. Vagnozzi, R.K. Kasam, M.A. Sargent, J.D. Molkentin, Cardiac cell therapy fails to rejuvenate the chronically scarred rodent heart, Circulation 144 (4) (2021) 328–331.
[57] T.L. Laundos, F. Vasques-Nóvoa, R.N. Gomes, V. Sampaio-Pinto, P. Cruz, H. Cruz, J. M. Santos, R.N. Barcia, P. Pinto-do-Ó, D.S. Nascimento, Consistent long-term therapeutic efficacy of human umbilical cord matrix-derived mesenchymal stromal cells after myocardial infarction despite individual differences and transient engraftment, Front. Cell Dev. Biol. 9 (2021).

[58] K.C. Chua, C. Rusinaru, K. Reinier, A. Uy-Evanado, H. Chugh, K. Gunson, J. Jui, S. S. Chugh, Tpeak-to-Tend interval corrected for heart rate: a more precise measure of increased sudden death risk? Heart Rhythm 13 (11) (2016) 2181–2185.
[59] M.N. Niemeijer, M.E. van den Berg, J.W. Deckers, O.H. Franco, A. Hofman, J. A. Kors, B.H. Stricker, P.R. Rijnbeek, M. Eijgelsheim, Consistency of heart rate-QTc prolongation consistency and sudden cardiac death: the Rotterdam Study, Heart Rhythm 12 (10) (2015) 2078–2085.
[60] B.I. Jugdutt, Ventricular remodeling after infarction and the extracellular collagen matrix: when is enough enough? Circulation 108 (11) (2003) 1395–1403.
[61] P. Zhang, M. Shen, C. Fernandez-Patron, Z. Kassiri, ADAMs family and relatives in cardiovascular physiology and pathology, J. Mol. Cell. Cardiol. 93 (2016) 186–199.
[62] M. Shimazaki, K. Nakamura, I. Kii, T. Kashima, N. Amizuka, M. Li, M. Saito, K. Fukuda, T. Nishiyama, S. Kitajima, Y. Saga, M. Fukayama, M. Sata, A. Kudo, Periostin is essential for cardiac healing after acute myocardial infarction, J. Exp. Med. 205 (2) (2008) 295–303.
[63] J.J. Russell, L.A. Grisanti, S.M. Brown, C.A. Bailey, S.B. Bender, B. Chandrasekar, Reversion inducing cysteine rich protein with Kazal motifs and cardiovascular diseases: the RECKlessness of adverse remodeling, Cell. Signal. 83 (2021) 109993.
[64] P. Huebener, T. Abou-Khamis, P. Zymek, M. Bujak, X. Ying, K. Chatila, S. Haudek, G. Thakker, N.G. Frangogiannis, CD44 is critically involved in infarct healing by regulating the inflammatory and fibrotic response, J. Immunol. 180 (4) (2008) 2625–2633.
[65] M. Becirovic-Agic, U. Chalise, M.J. Daseke 2nd, S. Konfrst, J.D. Salomon, P. K. Mishra, M.L. Lindsey, Infarct in the heart: what's MMP-9 got to do with it? Biomolecules 11 (4) (2021).
[66] T. Wang, J. Tian, Y. Jin, VCAM1 expression in the myocardium is associated with the risk of heart failure and immune cell infiltration in myocardium, Sci. Rep. 11 (1) (2021) 19488.
[67] T. Iwamiya, B.D. Segard, Y. Matsuoka, T. Imamura, Human cardiac fibroblasts expressing VCAM1 improve heart function in postinfarct heart failure rat models by stimulating lymphangiogenesis, PLoS One 15 (9) (2020) e0237810.
[68] A. Hanna, N.G. Frangogiannis, The role of the TGF-beta superfamily in myocardial infarction, Front. Cardiovasc. Med. 6 (2019) 140.
[69] W. Parichatikanond, T. Luangmonkong, S. Mangmool, H. Kurose, Therapeutic targets for the treatment of cardiac fibrosis and cancer: focusing on TGF-beta signaling, Front. Cardiovasc. Med. 7 (2020) 34.
[70] J.M. Baughman, R. Nilsson, V.M. Gohil, D.H. Arlow, Z. Gauhar, V.K. Mootha, A computational screen for regulators of oxidative phosphorylation implicates SLIRP in mitochondrial RNA homeostasis, PLoS Genet. 5 (8) (2009) e1000590.
[71] S. Pradervand, H. Yasukawa, O.G. Muller, H. Kjekshus, T. Nakamura, T.R. St Amand, T. Yajima, K. Matsumura, H. Duplain, M. Iwatate, S. Woodard, T. Pedrazzini, J. Ross, D. Firsov, B.C. Rossier, M. Hoshijima, K.R. Chien, Small proline-rich protein 1A is a gp130 pathway- and stress-inducible cardioprotective protein, EMBO J. 23 (22) (2004) 4517–4525.
[72] C. Zhang, X. He, J. Zhao, Y. Cao, J. Liu, W. Liang, Y. Zhou, C. Wang, R. Xue, Y. Dong, C. Liu, Angiopoietin-like protein 7 and short-term mortality in acute heart failure, Cardiorenal Med. 10 (2) (2020) 116–124.
[73] J. Fan, L. Qiu, H. Shu, B. Ma, M. Hagenmueller, J.H. Riffel, S. Meryer, M. Zhang, S. E. Hardt, L. Wang, D.W. Wang, H. Qiu, N. Zhou, Recombinant frizzled1 protein attenuated cardiac hypertrophy after myocardial infarction via the canonical Wnt signaling pathway, Oncotarget 9 (3) (2018) 3069–3080.
[74] M.W. Bao, Z. Cai, X.J. Zhang, L. Li, X. Liu, N. Wan, G. Hu, F. Wan, R. Zhang, X. Zhu, H. Xia, H. Li, Dickkopf-3 protects against cardiac dysfunction and ventricular remodelling following myocardial infarction, Basic Res. Cardiol. 110 (3) (2015) 25.
[75] K. Andenaes, I.G. Lunde, N. Mohammadzadeh, C.P. Dahl, J.M. Aronsen, M. E. Strand, S. Palmero, I. Sjaastad, G. Christensen, K.V.T. Engebretsen, T. Tonnessen, The extracellular matrix proteoglycan fibromodulin is upregulated in clinical and experimental heart failure and affects cardiac remodeling, PLoS One 13 (7) (2018) e0201422.
[76] V. Stylianidis, K.C.M. Hermans, W.M. Blankesteijn, Wnt signaling in cardiac remodeling and heart failure, in: J. Bauersachs, J. Butler, P. Sandner (Eds.), Heart Failure, Springer International Publishing, Cham, 2017, pp. 371–393.
[77] X. Li, D. Zhao, Z. Guo, T. Li, M. Qili, B. Xu, M. Qian, H. Liang, X. E, S. Chege Gitau, L. Wang, L. Huangfu, Q. Wu, C. Xu, H. Shan, Overexpression of SerpinE2/protease nexin-1 contribute to pathological cardiac fibrosis via increasing collagen deposition, Sci. Rep. 6 (2016) 37635.
[78] J. Man, P. Barnett, V.M. Christoffels, Structure and function of the Nppa-Nppb cluster locus during heart development and disease, Cell. Mol. Life Sci. 75 (8) (2018) 1435–1444.
[79] M. Zurek, E. Johansson, M. Palmer, T. Albery, K. Johansson, K. Ryden-Markinhutha, Q.D. Wang, Neuregulin-1 induces cardiac hypertrophy and impairs cardiac performance in post-myocardial infarction rats, Circulation 142 (13) (2020) 1308–1311.
[80] A. Battistoni, S. Rubattu, M. Volpe, Circulating biomarkers with preventive, diagnostic and prognostic implications in cardiovascular diseases, Int. J. Cardiol. 157 (2) (2012) 160–168.
[81] I.A. Sergeeva, I.B. Hooijkaas, I. Van Der Made, W.M. Jong, E.E. Creemers, V. M. Christoffels, A transgenic mouse model for the simultaneous monitoring of ANF and BNP gene activity during heart development and disease, Cardiovasc. Res. 101 (1) (2014) 78–86.
[82] L. Dugaucquier, E. Feyen, L. Mateiu, T.A.M. Bruyns, G.W. De Keulenaer, V.F. M. Segers, The role of endothelial autocrine NRG1/ERBB4 signaling in cardiac remodeling, Am. J. Physiol. Heart Circ. Physiol. 319 (2) (2020) H443–H455.
[83] C.L. Galindo, E. Kasasbeh, A. Murphy, S. Ryzhov, S. Lenihan, F.A. Ahmad, P. Williams, A. Nunnally, J. Adcock, Y. Song, F.E. Harrell, T.L. Tran, T.J. Parry, J. Iaci, A. Ganguly, I. Feoktistov, M.K. Stephenson, A.O. Caggiano, D.B. Sawyer, J. H. Cleator, Anti-remodeling and anti-fibrotic effects of the neuregulin-1beta glial growth factor 2 in a large animal model of heart failure, J. Am. Heart Assoc. 3 (5) (2014) e000773.
[84] C.L. Galindo, S. Ryzhov, D.B. Sawyer, Neuregulin as a heart failure therapy and mediator of reverse remodeling, Curr. Heart Fail. Rep. 11 (1) (2014) 40–49.
[85] M. Kaur, P. Tappia, Metabolic shifts during cardiac hypertrophy, Clin. Lipidol. 4 (6) (2009) 725–729.
[86] D.H. Tran, Z.V. Wang, Glucose metabolism in cardiac hypertrophy and heart failure, J. Am. Heart Assoc. 8 (12) (2019) e012673.
[87] L. Nascimben, J.S. Ingwall, B.H. Lorell, I. Pinz, V. Schultz, K. Tornheim, R. Tian, Mechanisms for increased glycolysis in the hypertrophied rat heart, Hypertension 44 (5) (2004) 662–667.
[88] T. Su, K. Huang, K.G. Mathews, V.F. Scharf, S. Hu, Z. Li, B.N. Frame, J. Cores, P. U. Dinh, M.A. Daniele, F.S. Ligler, K. Cheng, Cardiac stromal cell patch integrated with engineered microvessels improves recovery from myocardial infarction in rats and pigs, ACS Biomater. Sci. Eng. 6 (11) (2020) 6309–6320.
[89] L. Gao, Z.R. Gregorich, W. Zhu, S. Mattapally, Y. Oduk, X. Lou, R. Kannappan, A. V. Borovjagin, G.P. Walcott, A.E. Pollard, V.G. Fast, X. Hu, S.G. Lloyd, Y. Ge, J. Zhang, Large cardiac muscle patches engineered from human induced-pluripotent stem cell-derived cardiac cells improve recovery from myocardial infarction in swine, Circulation 137 (16) (2018) 1712–1730.
[90] K. Huang, E.W. Ozpinar, T. Su, J. Tang, D. Shen, L. Qiao, S. Hu, Z. Li, H. Liang, K. Mathews, V. Scharf, D.O. Freytes, K. Cheng, An off-the-shelf artificial cardiac patch improves cardiac repair after myocardial infarction in rats and pigs, Sci. Transl. Med. 12 (538) (2020).
[91] C. Cristallini, G. Vaccari, N. Barbani, E. Cibrario Rocchietti, R. Barberis, M. Falzone, K. Cabiale, G. Perona, E. Bellotti, R. Rastaldo, S. Pascale, P. Pagliaro, C. Giachino, Cardioprotection of PLGA/gelatine cardiac patches functionalised with adenosine in a large animal model of ischaemia and reperfusion injury: a feasibility study, J Tissue Eng Regen Med 13 (7) (2019) 1253–1264.
[92] S. Clauss, C. Bleyer, D. Schuttler, P. Tomsits, S. Renner, N. Klymiuk, R. Wakili, S. Massberg, E. Wolf, S. Kaab, Animal models of arrhythmia: classic electrophysiology to genetically modified large animals, Nat. Rev. Cardiol. 16 (8) (2019) 457–475.
[93] T. Liu, Y. Hao, Z. Zhang, H. Zhou, S. Peng, D. Zhang, K. Li, Y. Chen, M. Chen, Advanced cardiac patches for the treatment of myocardial infarction, Circulation 149 (25) (2024) 2002–2020.